PHYSICS

Visualizing the strong field–induced molecular breakup of C_{60} via x-ray diffraction

Kirsten Schnorr[1,2]*†, Sven Augustin[1,2,3]*†, Ulf Saalmann[4], Georg Schmid[2], Arnaud Rouzée[5], Razib Obaid[6], Andre AlHaddad[1,7], Nora Berrah[6], Cosmin I. Blaga[3,8], Christoph Bostedt[1,7,9], Manuel Cardosa-Gutierrez[10], Gabriella Carini[11,12], Ryan Coffee[11], Louis F. DiMauro[8], Philip Hart[11], Yuta Ito[13], Katharina Kubicek[11,14,15,16], Yoshiaki Kumagai[13], Jochen Küpper[15,17,18], Yu Hang Lai[8], Hannes Lindenblatt[2], Ruth A. Livingstone[15,18], Severin Meister[2], Robert Moshammer[2], Koji Motomura[13], Thomas Möller[19], Kaz Nakahara[11], Timur Osipov[11], Gaurav Pandey[10], Dipanwita Ray[11], Francoise Remacle[10], Daniel Rolles[3], Jan Michael Rost[4], Ilme Schlichting[20], Rüdiger Schmidt[21], Simone Techert[14], Florian Trost[2], Kiyoshi Ueda[13], Joachim Ullrich[22], Marc J.J. Vrakking[5], Julian Zimmermann[19,23], Claus Peter Schulz[5]*, Thomas Pfeifer[2]*

Laser-driven dynamics in polyatomic molecules poses a complex many-body problem. Understanding intense light-matter interaction is crucial for steering intramolecular quantum dynamical processes. Here, we record time-resolved x-ray diffraction images of C_{60} molecules during and after their interaction with intense near-infrared fields, giving direct access to structural changes of the molecules and their fragmentation in real time. Tuning the intensity of the excitation pulses, we uncover a transition from a weak-field regime of excited but stable molecules to a high-field regime dominated by Coulomb explosion. In the transition region, the molecules expand by up to 50% of their initial size within just 140 fs, with major fragmentation only setting in afterward. This work demonstrates that x-ray diffractive imaging is capable of retrieving time-resolved structural information of large molecules reshaped by intense laser fields. Laser-driven fragmentation is a first step toward observing molecular processes modified by laser fields of increasing intensity.

INTRODUCTION

Lasers can steer chemical reactions through the manipulation of molecular potential-energy surfaces. This control exploits the dynamic Stark effect of molecules in strong optical laser fields (*1*, *2*). Light-induced potential-energy curves have first been observed in the 1990s in H_2^+ manifesting as softening (*3*) or hardening (*4*) of a molecular bond. Even conical intersections can be induced by light, allowing to control the outcome of chemical reactions, such as photodissociation (*5*) and photoisomerization (*6*). The larger the molecular system to be steered, the more important are direct imaging methods to observe the effect of such laser control.

Fullerenes (*7*, *8*) are prototype systems to study fundamental light-matter interaction processes such as energy dissipation by efficient coupling of many electronic and nuclear degrees of freedom spanning timescales from atto- to microseconds (*9*). The response of gaseous C_{60} molecules to intense femtosecond (fs) laser pulses keeps attracting substantial interest both experimentally (*10*–*12*) and theoretically (*13*, *14*). The ionization and fragmentation patterns of C_{60} following irradiation with intense laser fields show the simultaneous creation of stable highly charged C_{60}^{n+} ions (*15*) along with the fragmentation into, e.g., C^+, … , C_{11}^+ ions (*10*, *16*). The breakup of the carbon cage into smaller and smaller fragments is proposed to proceed via a complex chain of bond ruptures and formations, and other nuclear rearrangement reactions. Often, the interpretation of results involved dominant excitation of either the symmetric breathing $a_g(1)$ (*14*, *17*–*19*) or the oblate-prolate $h_g(1)$ (*15*, *20*, *21*) mode, with vibrational periods of 67 and 122 fs, respectively.

The experimental results have up to now been almost exclusively based on charged-particle spectroscopy techniques, detecting electrons and ions nano- to microseconds after the laser interaction. Thus, the formation of transient structures and reactions taking place on the way to the detector, such as electron-ion recombination, remain hidden, and information about neutral fragments is lost. Femtosecond time-resolved x-ray coherent imaging is able to overcome these limitations and has recently become feasible on dilute samples with the advent of free-electron lasers (FELs), which provide sufficiently short and intense x-ray pulses with ~10^{12} photons per pulse (*22*–*26*). Here, we use elastic x-ray scattering to image the response of a gas-phase C_{60} ensemble undergoing near-infrared (NIR) laser–induced deformations as a function of time, directly observing the initial expansion and subsequent fragmentation of the molecules.

[1]Paul Scherrer Institut, 5232 Villigen, Switzerland. [2]Max-Planck-Institut für Kernphysik, 69117 Heidelberg, Germany. [3]J.R. Macdonald Laboratory, Department of Physics, Kansas State University, Manhattan, KS 66506, USA. [4]Max-Planck-Institut für Physik komplexer Systeme, 01187 Dresden, Germany. [5]Max Born Institut, 12489 Berlin, Germany. [6]University of Connecticut, Storrs, CT 06269, USA. [7]Argonne National Laboratory, Argonne, IL 60439, USA. [8]The Ohio State University, Columbus, OH 43210, USA. [9]École Polytechnique Fédérale de Lausanne, 1015 Lausanne, Switzerland. [10]Theoretical Physical Chemistry, RU Molsys, University of Liege, 4000 Liege, Belgium. [11]SLAC National Accelerator Laboratory, Menlo Park, CA 94025, USA. [12]Brookhaven National Laboratory, Upton, NY 11973, USA. [13]IMRAM, Tohoku University, 980-8577 Sendai, Japan. [14]Deutsches Elektronen-Synchrotron DESY, 22607 Hamburg, Germany. [15]Centre for Ultrafast Imaging, Universität Hamburg, 22761 Hamburg, Germany. [16]Max-Planck-Institut für biophysikalische Chemie, 37077 Göttingen, Germany. [17]Department of Physics, Universität Hamburg, 22761 Hamburg, Germany. [18]Center for Free-Electron Laser Science, Deutsches Elektronen-Synchrotron, 22607 Hamburg, Germany. [19]Technische Universität Berlin, 10623 Berlin, Germany. [20]Max-Planck-Institut für Medizinische Forschung, 69120 Heidelberg, Germany. [21]Technische Universität Dresden, 01062 Dresden, Germany. [22]Physikalisch Technische Bundesanstalt, 38116 Braunschweig, Germany. [23]Eidgenössische Technische Hochschule Zürich, 8092 Zürich, Switzerland.
*Corresponding author. Email: kirsten.schnorr@psi.ch (K.S.); sven.augustin@psi.ch (S.A.); cps@mbi-berlin.de (C.P.S.); tpfeifer@mpi-hd.mpg.de (T.P.)
†These authors contributed equally to this work.

RESULTS

The experimental scheme we used in order to investigate the NIR-induced dynamics of C_{60} molecules is illustrated in Fig. 1. An NIR fs laser pulse with central wavelength of 800 nm ionizes the C_{60} molecules to a degree that can be adjusted by varying the NIR laser intensity. The NIR intensity was calibrated in situ using ion time-of-flight (TOF) spectra of ionized and fragmented C_{60} molecules. We monitor the structural rearrangement of the ionized molecules by time-resolved x-ray coherent imaging using an intense fs x-ray FEL pulse at a photon energy of 1.8 keV. Scattering images for each time delay have to be averaged over thousands of shots due to the low scattering cross section of gas-phase C_{60} molecules. More details on the experimental parameters can be found in the "Experiment" section under Materials and Methods, as well as the Supplementary Materials.

Since C_{60} molecules are spherical, we need a model that allows us to describe scattering off spherical objects to interpret our recorded scattering patterns. For this purpose, we perform Guinier fits to the averaged scattering patterns, a method that is routinely used in x-ray scattering to determine the size of molecules. We followed the description by Guinier and Fournet given in section 2.1.2.6 of (*27*), where scattering off different geometrical objects is derived. More details can be found in the "Guinier fit" section in the Supplementary Materials. The scattering intensity $I(q,R)$ for a spherical object is given by

$$I(q,R) = I_e(q)F^2(q,R) \tag{1}$$

$$\begin{aligned} F(q,R) &\stackrel{!}{=} F_{\text{Guinier}}(q,R) \\ &= \underbrace{V_{\text{sph}}(R)\rho_e(R)}_{N}\left[3\frac{\sin(qR)-qR\cos(qR)}{(qR)^3}\right] \end{aligned} \tag{2}$$

Here, q is the momentum transfer, R the radius of the scattering object, $V_{\text{sph}}(R)$ the volume of the target sphere and $\rho_e(R) = \frac{N}{V_{\text{sph}}(R)}$ the average electronic scatterer density of N scatterers. We can rewrite Eq. 1 introducing the Guinier amplitude A

$$I(q,R) = A\left[3\frac{\sin(qR)-qR\cos(qR)}{(qR)^3}\right]^2 \tag{3}$$

$$A = I_e(q)N^2 \tag{4}$$

which has a quadratic dependence to the number of scatterers N.

The spherical symmetry of C_{60} molecules in a strong laser field may be deformed to ellipsoidal with the symmetry axis being the laser-polarization direction. To account for deformation imposed by the laser pulse, we have used the Guinier fit for ellipsoidal objects in our analysis, where R becomes dependent of R_{pol} and R_{equ}, the two radii of an ellipse (cf. the "Guinier fit" section in the Supplementary Materials).

We perform Guinier fits to the ensemble-averaged diffraction patterns for each 10 fs time bin. In particular for large NIR intensities, molecules fragment and the shape of each individual molecule will no longer be spherical or ellipsoidal for positive delays (cf. Fig. 1). However, because of the averaging over multiple thousands shots and thus many orientations of the molecular breakup pattern, we assume that the ensemble-averaged fragmentation pattern adds up to being spherical or ellipsoidal. The fitted Guinier amplitude A (Fig. 2, A to D) is proportional to the amount of scattered photons per solid angle and thus gives a measure of the degree of fragmentation and ionization of the molecules. A breakup of an intact C_{60} molecule into multiple moieties reduces the number of scatterers N_i per moiety and in turn the Guinier amplitude A, which is proportional to N_i^2. The Guinier amplitude was normalized to that of intact molecules obtained for negative delays. The fitted Guinier radius R is proportional to the radius of the C_{60} molecules and was normalized to the ground-state radius, also determined from data taken for negative delays (Fig. 2, E to H). Figure 2 shows the delay-dependent Guinier amplitudes and radii for four different NIR intensities [referred to as perturbative ($2\times10^{13}\,\frac{\text{W}}{\text{cm}^2}$), low ($1\times10^{14}\,\frac{\text{W}}{\text{cm}^2}$), intermediate ($2\times10^{14}\,\frac{\text{W}}{\text{cm}^2}$), and high ($8\times10^{14}\,\frac{\text{W}}{\text{cm}^2}$)].

At the perturbative NIR intensity, no dynamical response is observed in the experimental x-ray scattering patterns (Fig. 2, A and E). The corresponding TOF spectrum in Fig. 3C contains mainly C_{60}^+ cations, but no charged fragments. While the TOF spectra can only give information about ions detected microseconds after the interaction has taken place, x-ray coherent imaging is sensitive to in situ structural changes of both neutral and charged particles. Thus, the absence of delay-dependent features in Fig. 2 (A and E) indicates that the molecular structure is not altered on a picosecond timescale irrespective of whether the molecules were ionized or remained neutral during the NIR interaction. At the low intensity, the measurements of the Guinier amplitude as a function the delay, shown in Fig. 2B, provide a remarkably different view on the NIR-induced C_{60} dynamics than does the NIR-induced ion TOF spectrum shown in Fig. 3D. The TOF spectrum at the low intensity (Fig. 3D) might give the impression that fragmentation is already the dominant relaxation pathway given the amount of charged fragments. In contrast, the small drop of <30% in the Guinier amplitude (Fig. 2B) shows that the majority of molecules remains intact within the observed delay range. This apparent discrepancy is explained by the

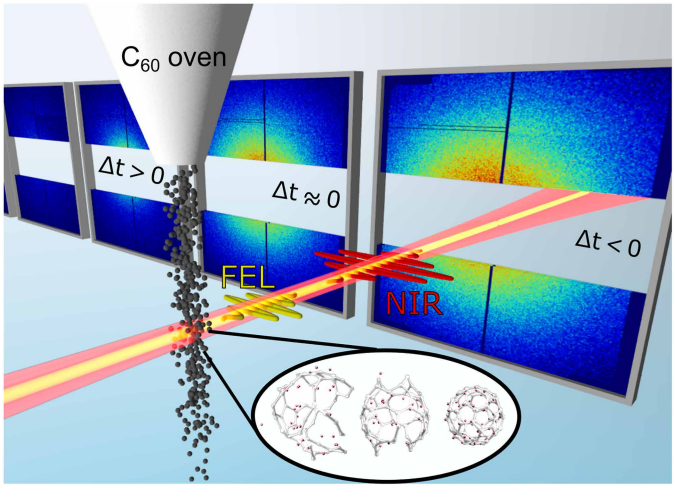

Fig. 1. Experimental scheme. An ensemble of C_{60} molecules is excited and ionized by an NIR pulse and probed by an FEL pulse via elastic x-ray scattering. Experimental scattering patterns at different delays Δt are shown for the intermediate NIR intensity. The inset contains three examples of computed structures resulting from the exposure to the NIR pulse.

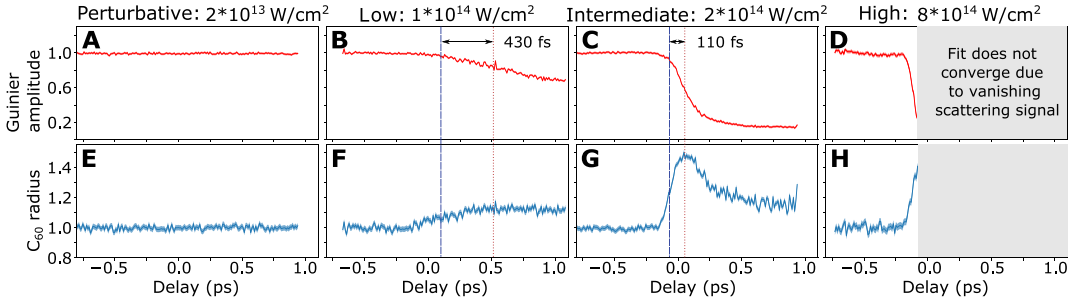

Fig. 2. Measured x-ray scattering signals as a function of NIR pump–x-ray probe delay. The normalized Guinier amplitude for the perturbative, low, intermediate and high NIR intensity (**A** to **D**) and the corresponding Guinier radii in units of the ground state C_{60} radius are plotted (**E** to **H**). Error bands indicate 1σ uncertainty (cf. the Supplementary Materials section "Uncertainty estimation"). Dashed blue lines mark the delays when the Guinier radii have increased to half of their maximal expansion and red dotted lines indicate the delays when the Guinier amplitudes have dropped to half of their respective minima.

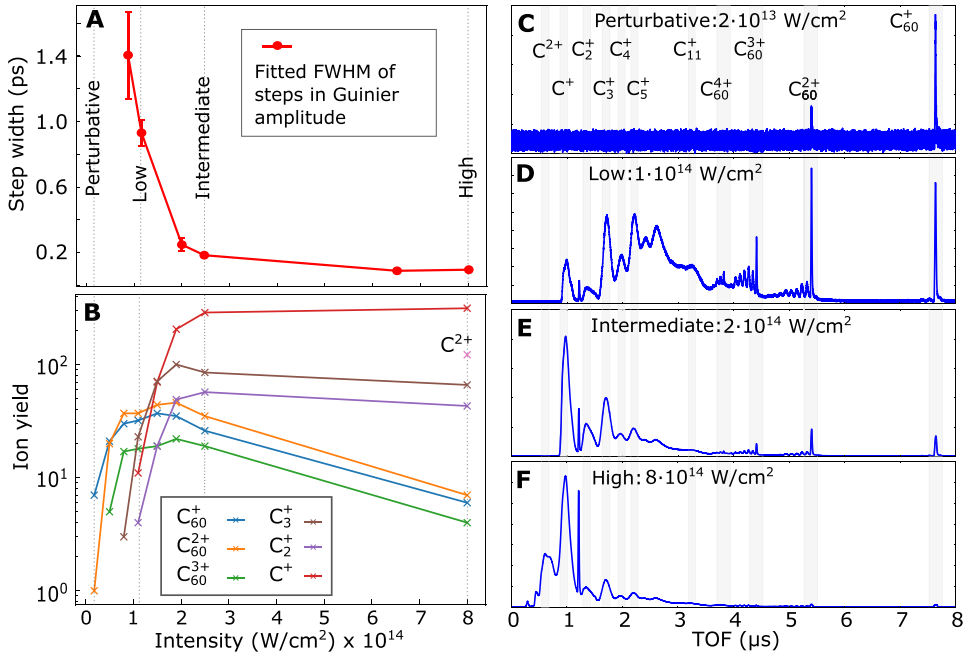

Fig. 3. NIR intensity-dependent dynamics. (**A**) FWHM of an error-function fit to the delay-dependent Guinier amplitude for different NIR intensities. (**B**) Charge-state yields from TOF spectra of selected ion species as a function of the NIR intensity. (**C** to **F**) TOF spectra recorded with only the NIR laser at the (C) perturbative, (D) low, (E) intermediate, and (F) high NIR intensity. Characteristic fragments are labeled on top of the respective peaks. The progression of peaks toward the small TOF side of the C_{60} cations corresponds to cations which have lost a single or multiple C_2 fragments (*11*). The sharp peak between C^+ and C_2^+ corresponds to H_2O^+ from ionization of residual gas.

fact that the TOF measurement is substantially more sensitive to small charged fragments compared to fullerene species (*28*) and blind to neutral molecules and fragments.

From NIR intensities $1 \times 10^{14} \frac{\mathrm{W}}{\mathrm{cm}^2}$, the Guinier amplitude drops for positive NIR pump–x-ray probe delays by an amount and at a rate that increases with the NIR intensity (Fig. 2, B to D). This is due to ionization-induced disintegration of a growing number of molecules. Between the low and intermediate intensity, the amplitude drop is particularly pronounced (Fig. 3A) and levels out afterward. The strong contrast from predominantly stable molecules at the low intensity to mostly fragmented molecules at the intermediate intensity shows a behavior similar to ionization ignition in strong field–ionized atomic clusters (*29*). There, ionization and consequently fragmentation is strongly enhanced when the laser intensity reaches the single ionization threshold: A burst of electrons, driven by the laser field, recollides multiple times and drives avalanche ionization via electron impact (*30*). The TOF spectra show a corresponding transition from a majority of stable C_{60}^{n+} and larger fragment ions at the low intensity to predominantly small ionic fragments (C_2^+, C^+, etc.) at the intermediate intensity (Fig. 3B). Both the intensity-dependent Guinier amplitude step widths (Fig. 3A) and the small fragments yield (Fig. 3B) show their steepest descent and ascent, respectively, in the region between low and intermediate intensity supporting the ionization-ignition analogy. In addition, Coulomb explosion driven by cascade hopping of electrons could contribute to the fast amplitude drop (*31*).

At the high NIR intensity, the Guinier amplitude drops to the background level within ~100 fs, indicating that most molecules

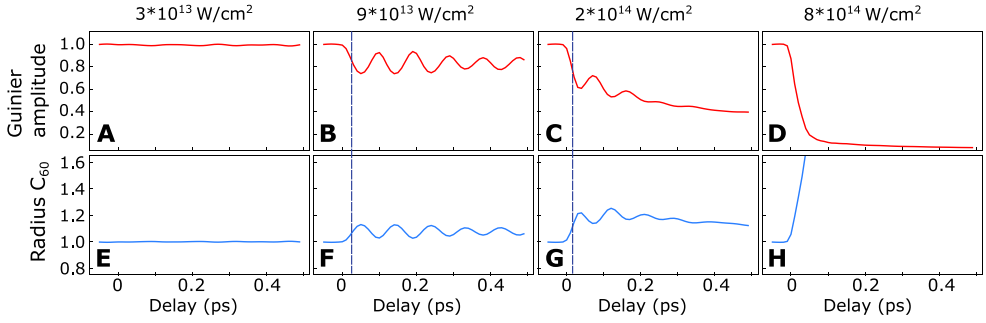

Fig. 4. Calculated delay-dependent scattering signals, masked with the same detector geometry and analyzed like the experimental data. The Guinier amplitude for the four different NIR intensities (**A** to **D**) are shown along with the corresponding Guinier radii in units of the ground state C_{60} radius (**E** to **H**). Dashed blue lines mark the delays when the Guinier radii have increased to half of their first oscillation maxima.

within the x-ray focus disintegrate completely within that time span. The large contribution of small fragments and the presence of doubly charged carbon ions in the TOF spectrum (Fig. 3, B and F) support a violent Coulomb explosion. The radius (Fig. 2H) expands simultaneously with the decreasing amplitude (Fig. 2D) until the size of the corresponding scattering patterns has reached the geometrical detection limit imposed by the gap in the scattering detector (cf. fig. S4). Likewise, the simulated dynamics is dominated by fast Coulomb explosion, which manifests in a rapid reduction of the scattering amplitude and a corresponding rapid increase in the radius (Fig. 4, D and H). Details about our classical molecular dynamics (MD) calculations can be found in the "Theory" sections in Materials and Methods and the Supplementary Materials. The calculated scattering signals were analyzed with the same fitting procedure as the experimental data including and masked with the detector geometry.

In the C_{60} dynamics, three cases can be identified: Bookended by the perturbative intensity, where amplitude and radius are both constant, and the high intensity, where the Guinier amplitude decreases simultaneously with the increase of the radius, the transition region of the low and intermediate intensities is characterized by a more complex expansion dynamics: The Guinier amplitudes drop with a delay and slower than the radii expand. While the radii expand to 50% of their respective maxima (marked as dashed blue lines in Fig. 2, F and G), the Guinier amplitudes drop by only 5% (Fig. 2B) and 10% (Fig. 2C) for the low and intermediate intensities, respectively. Thus, the differences in the dynamics of the radius expansion and the amplitude drop are intensity dependent: For the low intensity, the amplitude drops delayed by 430 fs (Fig. 2B) with respect to the radius expansion. Furthermore, the amplitude drop takes double the time [900 fs full width at half maximum (FWHM)] compared to the radius expansion (450 fs FWHM) (Fig. 3A). For the intermediate intensity, the delay of the amplitude drop reduces to 110 fs (Fig. 2C) and the expansion takes place within 140 fs, while the amplitude drops within 190 fs (Fig. 3A). The delayed drop of the amplitude with respect to the radius expansion indicates that the molecules undergo deformation and expansion before atomization sets in. In particular the small drop of the Guinier amplitude during the increase of the radius for the low intensity shows that the C_{60} molecules can at most undergo a heavily asymmetric breakup into a large moiety and small fragments. Since the reduction of the amplitude scales linearly with the number of fragments for symmetric breakup (cf. section "Relation between Guinier amplitude and molecular fragmentation" in the Supplementary Materials), a decrease of the amplitude of less than a factor of two is only possible for asymmetric fragmentation. Thus, for the intermediate intensity where the amplitude drops by 50% after the initial radius expansion, the most symmetric breakup possible is in two equally large moieties. The more likely scenario to reach the reduction by a factor two is however the formation of a large moiety during the expansion, where the amplitude drops by only 10% at half rise and a further asymmetric breakup when reaching the maximal radius. Breaking bonds of the C_{60} cage will produce initially large pieces, reducing the coherent scattering intensity only slightly and slowly before smaller fragments are formed, a hypothesis which would be in agreement with the experimental observation.

The intermediate intensity shows a remarkable additional feature: Following the fast expansion by a factor 1.5 within ~140 fs the radius shrinks again with a time constant of ~155 fs to 1.2 times the initial value (Fig. 2G and the "Fitting procedures" section in the Supplementary Materials). The decrease of the radius sets in when the Guinier amplitude has already decayed to half of its minimum. The strongly decreased Guinier amplitude during the radius drop indicates that a large fraction of molecules has already broken up. Thus, the reduced radius is a signature of scattering off small fragments. While is it likely that we excite Rydberg states, the observed MD can not be associated with the decay of these states since their lifetime is on the microsecond timescale (*32*).

The simulated Guinier amplitudes and radii (Fig. 4, B, C, F, and G) at large delays show good qualitative agreement with the experiment indicating that the asymptotic fragmentation patterns are well reproduced by our calculations. For the intermediate intensity, also the expansion of the radius with subsequent decrease is reproduced albeit with a smaller maximal radius. The delayed and slowed down drop of the Guinier amplitude with respect to the radius is however not present in the simulations. The most notable difference between the simulation and the measured data is the complete absence of the breathing mode oscillation in the experiment. The simulation for the low intensity predicts a substantial peak-to-peak amplitude of the oscillation of up to 20% for the Guinier amplitude and up to 10% for the radius. For the intermediate intensity, the simulated amplitude and radius (Fig. 4, C and G) are still clearly modulated by the breathing-mode oscillation but damped by fragmentation.

DISCUSSION

We have explored the underlying reasons for the discrepancy between the measured and predicted C_{60} expansion dynamics by adding ad-hoc terms to our classical theory model representing

possible effects that may arise through the interplay of a coupled quantum many-body electron-ion system. As low-lying quantum states cannot be included in the classical model, we approached their contribution in a statistical fashion by adding a constant heating term per time step to our MD calculations. This can be considered to represent a global energy increase of the molecules through interaction of the free (laser-driven) electrons with the ones still quantum-mechanically bound and contributing to bonding and thus strongly couple to the positions of the ions/nuclei. By doing so, we find an earlier onset of Coulomb explosion and stronger damping of the oscillation (cf. "Theory" section in the Supplementary Materials). Depending on the heating conditions, the oscillation can be completely suppressed. Our coarse-grained approach to include multi-electron heating as a factor is a first step in understanding the coupling of electrons to nuclear motion in a complex quantum system, hereby studying its influence on the predicted breathing mode. By including this new mechanism in our modeling, we find that electronic heating on timescales faster than vibrations can suppress coherent internuclear motion. It may thus be the reason for the absence in the experiment with far-reaching implications for understanding and controlling in general complex systems exposed to lasers.

Most calculations have identified the excitation of the symmetric breathing (*18*) or the oblate-prolate (*13*, *20*) mode to be the crucial step to efficiently couple electronic excitation to nuclear degrees of freedom in C_{60}, even under violent fragmentation conditions (*14*). Our experimental data shows no such periodic changes. Direct experimental evidence of the excitation of the breathing mode is sparse. It has been reported for a solid-state C_{60} sample (*19*) and in a gas-phase experiment, in the latter case by applying shaped laser pulses optimized to create vibrationally hot fragments (*17*). The interpretation of other experimental results, like the complex fragmentation (*15*) or deformation (*21*) of C_{60} molecules in strong fs laser pulses, has been based on the dominant excitation of one vibrational mode. In contrast to the majority of previous gas-phase experiments on C_{60}, which applied techniques highly selective to specific charged fragments, we image the response of the full ensemble using x-ray scattering. Our results suggest that the vibrational coupling is not as selective as proposed by theory.

The poor agreement of simulation and experiment at small delays for the low and intermediate intensity shows that the current level of theory is not able to capture the complex multi-electron dynamics taking place during the interaction with a strong fs laser field. In particular, transient highly excited and ionized states, which decay via transfer processes faster than vibrational timescales, are not included in our calculations. Currently, a full quantum mechanical treatment including all intramolecular relaxation processes is technically not feasible. Thus, our combined experimental and theoretical study on strong field–ionized C_{60} serves as ideal test ground to develop the necessary fundamental understanding of multi-electron dynamics in highly excited polyatomic molecular systems, which are needed to control chemical reactions with laser fields.

In conclusion, we have imaged the strong field–induced dynamics of an ensemble of gas-phase C_{60} molecules using fs time-resolved x-ray diffraction. In the laser intensity transition regime between mostly stable and violently Coulomb-exploding molecules, the MD is governed by a fast expansion, which facilitates disintegration of the molecules afterward. This experiment demonstrates the feasibility of imaging laser-driven MD, which, as a typically nonresonant excitation process, triggers a plethora of different fragmentation processes and manipulates the system under investigation itself. Because of the low scattering cross sections of single molecules, our method required averaging over many shots and allows to retrieve only the structure of an ensemble of molecules. Similar ensemble-averaged data have been used to observe photochemical reactions using hard x-ray scattering where methods for structure retrieval are under development [e.g., (*23*–*26*)]. In contrast, e.g., x-ray–induced Coulomb-explosion imaging allows to retrieve structural information on a single-molecule level but is so far limited to smaller molecules and low laser intensities (*33*–*35*). Furthermore, x-ray imaging of strong field–driven MD as introduced here could be improved in the future by using nanofocusing technologies (*36*). Thus, this work lays the foundation to not only observe chemistry as it happens, but also to drive chemical reactions by intense laser fields using x-ray diffraction as a probe.

MATERIALS AND METHODS

Experiment

The experiments were conducted at the Linac Coherent Light Source (*37*) at the AMO endstation (*38*) with a photon energy of 1.8 keV ($\lambda_{FEL} = 0.69$ nm) and intensities of $\sim 10^{16} \frac{W}{cm^2}$. The collinear NIR ($\lambda_{NIR} = 800$ nm) and x-ray beams were focused down to diameters of ~60 (FWHM) and ~20 μm (FWHM), respectively, and intersected the center of a C_{60} beam (Fig. 1). The NIR intensity was varied between $2 \times 10^{13} \frac{W}{cm^2}$ and $8 \times 10^{14} \frac{W}{cm^2}$. C_{60} molecules were evaporated from an oven heated to 870 K, producing a sample density at the laser focus of $\sim 10^{11}$ particles/cm^3. After the interaction, both laser pulses passed through a gap in the large-area pnCCD detector that recorded the scattered x-rays. Scattering patterns were recorded as a function of the NIR-pump–x-ray-probe delay over a range of ±1 ps, where positive delays denote that the NIR pulses preceded the x-ray pulses (Fig. 2). Delay scans were repeated over 1 to 2 hours at 120 Hz repetition rate for each NIR intensity. The NIR intensity and the corresponding C_{60} ionization and fragmentation patterns were characterized with an ion TOF spectrometer. An independent TOF-based NIR/x-ray cross-correlation measurement on N_2 yielded an instrument response function of 38 ± 3 fs (FWHM) with jitter correction using a time tool and was used to determine the time overlap (section "Experimental procedures" in the Supplementary Materials). The pulse durations of the x-ray and NIR laser pulses were both estimated to be 30 fs.

Theory

The NIR-induced dynamics was calculated with classical MD simulations describing the laser-driven motion of electrons and ions (cf. the section "Theory" in the Supplementary Materials). These calculations are based on empirical two- and three-body forces (*39*) augmented by pairwise Coulomb interactions. Whereas the former account for the covalent bonds in C_{60}, the latter are essential for describing multiply charged C_{60}. With one active electron per atom, we include electron-electron collisions, electron screening of C ions, and Coulomb explosion of the ions. From the results of the MD calculations, x-ray scattering images were simulated using the experimental beam parameters and geometries and analyzed like the experimental data (Fig. 4). In addition, quantum dynamics simulations (cf. the section "Theory" in the Supplementary Materials) were carried out for the low intensity regime.

Supplementary Materials

The PDF file includes:

Supplementary Text
Figs. S1 to S8
Legends for movies S1 to S4
References

Other Supplementary Material for this manuscript includes the following:

Movies S1 to S4

REFERENCES AND NOTES

1. A. D. Bandrauk, *Molecules in Laser Fields* (Springer Netherlands, Dordrecht, 1995), pp. 131–150.
2. B. J. Sussman, D. Townsend, M. Y. Ivanov, A. Stolow, Dynamic stark control of photochemical processes. *Science* **314**, 278 (2006).
3. P. H. Bucksbaum, A. Zavriyev, H. G. Muller, D. W. Schumacher, Softening of the H_2^+ molecular bond in intense laser fields. *Phys. Rev. Lett.* **64**, 1883 (1990).
4. L. J. Frasinski, J. H. Posthumus, J. Plumridge, K. Codling, P. F. Taday, A. J. Langley, Manipulation of bond hardening in H_2^+ by chirping of intense femtosecond laser pulses. *Phys. Rev. Lett.* **83**, 3625 (1999).
5. M. E. Corrales, J. González-Vázquez, G. Balerdi, I. R. Solá, R. de Nalda, L. Bañares, Control of ultrafast molecular photodissociation by laser-field-induced potentials. *Nat. Chem.* **6**, 785 (2014).
6. J. Kim, H. Tao, J. L. White, V. S. Petrović, T. J. Martinez, P. H. Bucksbaum, Control of 1,3-cyclohexadiene photoisomerization using light-induced conical intersections. *J. Phys. Chem. A* **116**, 2758–2763 (2012).
7. H. W. Kroto, J. R. Heath, S. C. O'Brien, R. F. Curl, R. E. Smalley, C_{60}: Buckminsterfullerene. *Nature* **318**, 162 EP (1985).
8. W. Krätschmer, L. D. Lamb, K. Fostiropoulos, D. R. Huffman, Solid C_{60}: A new form of carbon. *Nature* **347**, 354–358 (1990).
9. F. Lépine, Multiscale dynamics of C_{60} from attosecond to statistical physics. *J. Phys. B At. Mol. Opt. Phys.* **48**, 122002 (2015).
10. E. E. B. Campbell, K. Hansen, K. Hoffmann, G. Korn, M. Tchaplyguine, M. Wittmann, I. V. Hertel, From above threshold ionization to statistical electron emission: The laser pulse-duration dependence of C_{60} photoelectron spectra. *Phys. Rev. Lett.* **84**, 2128 (2000).
11. I. V. Hertel, T. Laarmann, C. P. Schulz, Ultrafast excitation, ionization, and fragmentation of C_{60}. *Adv. Atom. Mol. Optic. Phys.* **50**, 219–286 (2005).
12. N. Berrah, A. Sanchez-Gonzalez, Z. Jurek, R. Obaid, H. Xiong, R. J. Squibb, T. Osipov, A. Lutman, L. Fang, T. Barillot, J. D. Bozek, J. Cryan, T. J. A. Wolf, D. Rolles, R. Coffee, K. Schnorr, S. Augustin, H. Fukuzawa, K. Motomura, N. Niebuhr, L. J. Frasinski, R. Feifel, C. P. Schulz, K. Toyota, S. K. Son, K. Ueda, T. Pfeifer, J. P. Marangos, R. Santra, Femtosecond-resolved observation of the fragmentation of buckminsterfullerene following x-ray multiphoton ionization. *Nat. Phys.* **15**, 1279–1283 (2019).
13. G. P. Zhang, T. F. George, Controlling vibrational excitations in C_{60} by laser pulse durations. *Phys. Rev. Lett.* **93**, 147401 (2004).
14. M. Fischer, J. Handt, G. Seifert, R. Schmidt, Orientation dependence of energy absorption and relaxation dynamics of C_{60} in fs-laser pulses. *Phys. Rev. A* **88**, 061403 (2013).
15. V. R. Bhardwaj, P. B. Corkum, D. M. Rayner, Internal laser-induced dipole force at work in C_{60} molecule. *Phys. Rev. Lett.* **91**, 203004 (2003).
16. M. Boyle, T. Laarmann, I. Shchatsinin, C. P. Schulz, I. V. Hertel, Fragmentation dynamics of fullerenes in intense femtosecond-laser fields: Loss of small neutral fragments on a picosecond time scale. *J. Chem. Phys.* **122**, 181103 (2005).
17. T. Laarmann, I. Shchatsinin, A. Stalmashonak, M. Boyle, N. Zhavoronkov, J. Handt, R. Schmidt, C. P. Schulz, I. V. Hertel, Control of giant breathing motion in C_{60} with temporally shaped laser pulses. *Phys. Rev. Lett.* **98**, 058302 (2007).
18. H. O. Jeschke, M. E. Garcia, J. Alonso, Nonthermal fragmentation of C_{60}. *Chem. Phys. Lett.* **352**, 154–162 (2002).
19. S. L. Dexheimer, D. M. Mittleman, R.W. Schoenlein, W. Vareka, X.-D. Xiang, A. Zettl, C.V. Shank, "Ultrafast dynamics of solid C_{60}," in *Eighth International Conference on Ultrafast Phenomena*. Technical Digest Series (Optica Publishing Group, 1992).
20. K. Nakai, H. Kono, Y. Sato, N. Niitsu, R. Sahnoun, M. Tanaka, Y. Fujimura, Ab initio molecular dynamics and wavepacket dynamics of highly charged fullerene cations produced with intense near-infrared laser pulses. *Chem. Phys.* **338**, 127–134 (2007).
21. H. Fuest, Y. H. Lai, C. I. Blaga, K. Suzuki, J. Xu, P. Rupp, H. Li, P. Wnuk, P. Agostini, K. Yamazaki, M. Kanno, H. Kono, M. F. Kling, L. F. DiMauro, Diffractive imaging of C_{60} structural deformations induced by intense femtosecond midinfrared laser fields. *Phys. Rev. Lett.* **122**, 053002 (2019).
22. T. Gorkhover, S. Schorb, R. Coffee, M. Adolph, L. Foucar, D. Rupp, A. Aquila, J. D. Bozek, S. W. Epp, B. Erk, L. Gumprecht, L. Holmegaard, A. Hartmann, R. Hartmann, G. Hauser, P. Holl, A. Hömke, P. Johnsson, N. Kimmel, K.-U. Kühnel, M. Messerschmidt, C. Reich, A. Rouzée, B. Rudek, C. Schmidt, J. Schulz, H. Soltau, S. Stern, G. Weidenspointner, B. White, J. Küpper, L. Strüder, I. Schlichting, J. Ullrich, D. Rolles, A. Rudenko, T. Möller, C. Bostedt, Femtosecond and nanometre visualization of structural dynamics in superheated nanoparticles. *Nat. Photon.* **10**, 93–97 (2016).
23. M. P. Minitti, J. M. Budarz, A. Kirrander, J. S. Robinson, D. Ratner, T. J. Lane, D. Zhu, J. M. Glownia, M. Kozina, H. T. Lemke, M. Sikorski, Y. Feng, S. Nelson, K. Saita, B. Stankus, T. Northey, J. B. Hastings, P. M. Weber, Imaging molecular motion: Femtosecond x-ray scattering of an electrocyclic chemical reaction. *Phys. Rev. Lett.* **114**, 255501 (2015).
24. J. M. Glownia, A. Natan, J. P. Cryan, R. Hartsock, M. Kozina, M. P. Minitti, S. Nelson, J. Robinson, T. Sato, T. van Driel, G. Welch, C. Weninger, D. Zhu, P. H. Bucksbaum, Self-referenced coherent diffraction x-ray movie of ångstrom- and femtosecond-scale atomic motion. *Phys. Rev. Lett.* **117**, 153003 (2016).
25. K. Haldrup, G. Levi, E. Biasin, P. Vester, M. G. Laursen, F. Beyer, K. S. Kjær, T. Brandt van Driel, T. Harlang, A. O. Dohn, R. J. Hartsock, S. Nelson, J. M. Glownia, H. T. Lemke, M. Christensen, K. J. Gaffney, N. E. Henriksen, K. B. Møller, M. M. Nielsen, Ultrafast x-ray scattering measurements of coherent structural dynamics on the ground-state potential energy surface of a diplatinum molecule. *Phys. Rev. Lett.* **122**, 063001 (2019).
26. B. Stankus, H. Yong, N. Zotev, J. M. Ruddock, D. Bellshaw, T. J. Lane, M. Liang, S. Boutet, S. Carbajo, J. S. Robinson, W. du, N. Goff, Y. Chang, J. E. Koglin, M. P. Minitti, A. Kirrander, P. M. Weber, Ultrafast x-ray scattering reveals vibrational coherence following rydberg excitation. *Nat. Chem.* **11**, 716–721 (2019).
27. A. Guinier, G. Fournet, *Small-Angle Scattering of X-rays* (John Wiley & Sons, Inc., New York, 1st ed., 1955).
28. R. Ehlich, M. Westerburg, E. E. B. Campbell, Fragmentation of fullerenes in collisions with atomic and molecular targets. *J. Chem. Phys.* **104**, 1900–1911 (1996).
29. C. Rose-Petruck, K. J. Schafer, K. R. Wilson, C. P. J. Barty, Ultrafast electron dynamics and inner-shell ionization in laser driven clusters. *Phys. Rev. A* **55**, 1182–1190 (1997).
30. P. B. Corkum, Plasma perspective on strong field multiphoton ionization. *Phys. Rev. Lett.* **71**, 1994–1997 (1993).
31. J. Kou, V. Zhakhovskii, S. Sakabe, K. Nishihara, S. Shimizu, S. Kawato, M. Hashida, K. Shimizu, S. Bulanov, Y. Izawa, Y. Kato, N. Nakashima, Anisotropic coulomb explosion of C_{60} irradiated with a high-intensity femtosecond laser pulse. *J. Chem. Phys.* **112**, 5012–5020 (2000).
32. E. E. B. Campbell, R. D. Levine, Delayed ionization and fragmentation en route to thermionic emission: Statistics and dynamics. *Annu. Rev. Phys. Chem.* **51**, 65–98 (2000).
33. R. Boll, J. M. Schäfer, B. Richard, K. Fehre, G. Kastirke, Z. Jurek, M. S. Schöffler, M. M. Abdullah, N. Anders, T. M. Baumann, S. Eckart, B. Erk, A. de Fanis, R. Dörner, S. Grundmann, P. Grychtol, A. Hartung, M. Hofmann, M. Ilchen, L. Inhester, C. Janke, R. Jin, M. Kircher, K. Kubicek, M. Kunitski, X. Li, T. Mazza, S. Meister, N. Melzer, J. Montano, V. Music, G. Nalin, Y. Ovcharenko, C. Passow, A. Pier, N. Rennhack, J. Rist, D. E. Rivas, D. Rolles, I. Schlichting, L. P. H. Schmidt, P. Schmidt, J. Siebert, N. Strenger, D. Trabert, F. Trinter, I. Vela-Perez, R. Wagner, P. Walter, M. Weller, P. Ziolkowski, S. K. Son, A. Rudenko, M. Meyer, R. Santra, T. Jahnke, X-ray multiphoton-induced Coulomb explosion images complex single molecules. *Nat. Phys.* **18**, 423–428 (2022).
34. X. Li, R. Boll, P. Vindel-Zandbergen, J. González-Vázquez, D. E. Rivas, S. Bhattacharyya, K. Borne, K. Chen, A. de Fanis, B. Erk, R. Forbes, A. E. Green, M. Ilchen, B. Kaderiya, E. Kukk, H. V. S. Lam, T. Mazza, T. Mullins, B. Senfftleben, F. Trinter, S. Usenko, A. S. Venkatachalam, E. Wang, J. P. Cryan, M. Meyer, T. Jahnke, P. J. Ho, D. Rolles, A. Rudenko, Imaging a light-induced molecular elimination reaction with an X-ray free-electron laser. *Nat. Commun.* **16**, 7006 (2025).
35. B. Richard, R. Boll, S. Banerjee, J. M. Schäfer, Z. Jurek, G. Kastirke, K. Fehre, M. S. Schöffler, N. Anders, T. M. Baumann, S. Eckart, B. Erk, A. de Fanis, R. Dörner, S. Grundmann, P. Grychtol, M. Hofmann, M. Ilchen, M. Kircher, K. Kubicek, M. Kunitski, X. Li, T. Mazza, S. Meister, N. Melzer, J. Montano, V. Music, Y. Ovcharenko, C. Passow, A. Pier, N. Rennhack, J. Rist, D. E. Rivas, D. Rolles, I. Schlichting, L. P. H. Schmidt, P. Schmidt, D. Trabert, F. Trinter, R. Wagner, P. Walter, P. Ziolkowski, A. Rudenko, M. Meyer, R. Santra, L. Inhester, T. Jahnke, Imaging collective quantum fluctuations of the structure of a complex molecule. *Science* **389**, 650–654 (2025).
36. Y. Inubushi, G. Yamaguchi, J. Yamada, Y. Kubota, I. Inoue, T. Osaka, T. Yabuuchi, K. Tono, M. Yabashi, Development of portable nanofocusing optics for X-ray free-electron laser pulses. *J. Synchrotron Rad.* **32**, 534–538 (2025).
37. P. Emma, R. Akre, J. Arthur, R. Bionta, C. Bostedt, J. Bozek, A. Brachmann, P. Bucksbaum, R. Coffee, F. J. Decker, Y. Ding, D. Dowell, S. Edstrom, A. Fisher, J. Frisch, S. Gilevich, J. Hastings, G. Hays, P. Hering, Z. Huang, R. Iverson, H. Loos, M. Messerschmidt, A. Miahnahri, S. Moeller, H. D. Nuhn, G. Pile, D. Ratner, J. Rzepiela, D. Schultz, T. Smith, P. Stefan, H. Tompkins, J. Turner, J. Welch, W. White, J. Wu, G. Yocky, J. Galayda, First lasing and operation of an ångstrom-wavelength free-electron laser. *Nat. Photon.* **4**, 641–647 (2010).
38. T. Osipov, C. Bostedt, J. C. Castagna, K. R. Ferguson, M. Bucher, S. C. Montero, M. L. Swiggers, R. Obaid, D. Rolles, A. Rudenko, J. D. Bozek, N. Berrah, The lamp instrument at the linac coherent light source free-electron laser. *Rev. Sci. Instrum.* **89**, 035112 (2018).
39. J. Tersoff, Modeling solid-state chemistry: Interatomic potentials for multicomponent systems. *Phys. Rev. B* **39**, 5566–5568 (1989).

40. K. R. Ferguson, M. Bucher, J. D. Bozek, S. Carron, J. C. Castagna, R. Coffee, G. I. Curiel, M. Holmes, J. Krzywinski, M. Messerschmidt, M. Minitti, A. Mitra, S. Moeller, P. Noonan, T. Osipov, S. Schorb, M. Swiggers, A. Wallace, J. Yin, C. Bostedt, The atomic, molecular and optical science instrument at the linac coherent light source. *J. Synchrotron Radiat.* **22**, 492–497 (2015).
41. L. Strüder, S. Epp, D. Rolles, R. Hartmann, P. Holl, G. Lutz, H. Soltau, R. Eckart, C. Reich, K. Heinzinger, C. Thamm, A. Rudenko, F. Krasniqi, K. U. Kühnel, C. Bauer, C. D. Schröter, R. Moshammer, S. Techert, D. Miessner, M. Porro, O. Hälker, N. Meidinger, N. Kimmel, R. Andritschke, F. Schopper, G. Weidenspointner, A. Ziegler, D. Pietschner, S. Herrmann, U. Pietsch, A. Walenta, W. Leitenberger, C. Bostedt, T. Möller, D. Rupp, M. Adolph, H. Graafsma, H. Hirsemann, K. Gärtner, R. Richter, L. Foucar, R. L. Shoeman, I. Schlichting, J. Ullrich, Large-format, high-speed, x-ray pnCCDs combined with electron and ion imaging spectrometers in a multipurpose chamber for experiments at 4th generation light sources. *Nucl. Instrum. Methods Phys. Res. A* **614**, 483–496 (2010).
42. M. P. Minitti, J. S. Robinson, R. N. Coffee, S. Edstrom, S. Gilevich, J. M. Glownia, E. Granados, P. Hering, M. C. Hoffmann, A. Miahnahri, D. Milathianaki, W. Polzin, D. Ratner, F. Tavella, S. Vetter, M. Welch, W. E. White, A. R. Fry, Optical laser systems at the Linac Coherent Light Source. *J. Synchrotron Radiat.* **22**, 526–531 (2015).
43. X. Lu, L. Feng, T. Akasaka, S. Nagase, Current status and future developments of endohedral metallofullerenes. *Chem. Soc. Rev.* **41**, 7723–7760 (2012).
44. K. R. Ferguson, M. Bucher, T. Gorkhover, S. Boutet, H. Fukuzawa, J. E. Koglin, Y. Kumagai, A. Lutman, A. Marinelli, M. Messerschmidt, K. Nagaya, J. Turner, K. Ueda, G. J. Williams, P. H. Bucksbaum, C. Bostedt, Transient lattice contraction in the solid-to-plasma transition. *Sci. Adv.* **2**, e1500837 (2016).
45. K. R. Ferguson, Crystal structure determination of xenon nanoparticles and x-ray induced transient lattice contraction in the solid-to-plasma transition, Ph.D. thesis, Stanford University (2016). https://stacks.stanford.edu/file/druid:qk328xg1417/Submitted-Dissertation-augmented.pdf.
46. M. Harmand, R. Coffee, M. R. Bionta, M. Chollet, D. French, D. Zhu, D. M. Fritz, H. T. Lemke, N. Medvedev, B. Ziaja, S. Toleikis, M. Cammarata, Achieving few-femtosecond time-sorting at hard x-ray free-electron lasers. *Nat. Photon.* **7**, 215–218 (2013).
47. S. Schorb, T. Gorkhover, J. P. Cryan, J. M. Glownia, M. R. Bionta, R. N. Coffee, B. Erk, R. Boll, C. Schmidt, D. Rolles, A. Rudenko, A. Rouzee, M. Swiggers, S. Carron, J. C. Castagna, J. D. Bozek, M. Messerschmidt, W. F. Schlotter, C. Bostedt, X-ray–optical cross-correlator for gas-phase experiments at the Linac Coherent Light Source free-electron laser. *Appl. Phys. Lett.* **100**, 121107 (2012).
48. B. F. Murphy, T. Osipov, Z. Jurek, L. Fang, S. K. Son, M. Mucke, J. H. D. Eland, V. Zhaunerchyk, R. Feifel, L. Avaldi, P. Bolognesi, C. Bostedt, J. D. Bozek, J. Grilj, M. Guehr, L. J. Frasinski, J. Glownia, D. T. Ha, K. Hoffmann, E. Kukk, B. K. McFarland, C. Miron, E. Sistrunk, R. J. Squibb, K. Ueda, R. Santra, N. Berrah, Femtosecond x-ray-induced explosion of C_{60} at extreme intensity. *Nat. Comm.* **5**, 4281 (2014).
49. U. Saalmann, C. Siedschlag, J. M. Rost, Topical review: Mechanisms of cluster ionization in strong laser pulses. *J. Phys. B At. Mol. Opt. Phys.* **39**, R39 (2006).
50. S. G. Kim, D. Tománek, Melting the fullerenes: A molecular dynamics study. *Phys. Rev. Lett.* **72**, 2418–2421 (1994).
51. A. D. Bandrauk, S. Chelkowski, N. H. Shon, Measuring the electric field of few-cycle laser pulses by attosecond cross correlation. *Phys. Rev. Lett.* **89**, 283903 (2002).
52. H. Li, B. Mignolet, G. Wachter, S. Skruszewicz, S. Zherebtsov, F. Süßmann, A. Kessel, S. A. Trushin, N. G. Kling, M. Kübel, B. Ahn, D. Kim, I. Ben-Itzhak, C. L. Cocke, T. Fennel, J. Tiggesbäumker, K. H. Meiwes-Broer, C. Lemell, J. Burgdörfer, R. D. Levine, F. Remacle, M. F. Kling, Coherent electronic wave packet motion in C_{60} controlled by the waveform and polarization of few-cycle laser fields. *Phys. Rev. Lett.* **114**, 123004 (2015).
53. B. Mignolet, R. D. Levine, F. Remacle, Control of electronic dynamics visualized by angularly resolved photoelectron spectra: A dynamical simulation with an IR pump and xuv attosecond-pulse-train probe. *Phys. Rev. A* **89**, 021403 (2014).
54. T. Yanai, Y. Kurashige, D. Ghosh, G. K.-L. Chan, Accelerating convergence in iterative solution for large-scale complete active space self-consistent-field calculations. *Int. J. Quantum Chem.* **109**, 2178–2190 (2009).
55. B. Mignolet, J. O. Johansson, E. E. B. Campbell, F. Remacle, Probing rapidly-ionizing super-atom molecular orbitals in C_{60}: A computational and femtosecond photoelectron spectroscopy study. *ChemPhysChem* **14**, 3332–3340 (2013).
56. B. Mignolet, R. D. Levine, F. Remacle, Localized electron dynamics in attosecond-pulse-excited molecular systems: Probing the time-dependent electron density by sudden photoionization. *Phys. Rev. A* **86**, 053429 (2012).
57. G. M. Seabra, I. G. Kaplan, V. G. Zakrzewski, J. V. Ortiz, Electron propagator theory calculations of molecular photoionization cross sections: The first-row hydrides. *J. Chem. Phys.* **121**, 4143–4155 (2004).

Acknowledgments: We thank the LCLS staff for optimal beamtime conditions and B. Mignolet for discussions. **Funding:** K.S. acknowledges support through Starting Grant TMSGI2_211288 from the Swiss National Science Foundation. K.S. and K.K. thank the Volkswagen Foundation for awarding them a Peter Paul Ewald fellowship. S.A. acknowledges the European Union's Horizon 2020 research and innovation program under the Marie Sklodowska-Curie grant agreement no. 701647 for awarding a fellowship. S.A. and D.Ro. thank the US Department of Energy, Office of Science, Basic Energy Sciences, Chemical Sciences, Geosciences, and Biosciences Division under contract no. DEFG02-86ER13491 for support. R.O. and N.B. acknowledge support from the Chemical Sciences, Geosciences and Biosciences Division, Office of Basic Energy Sciences, Office of Science, US Department of Energy, grant no DE-SC0012376. C.I.B. thanks the US Department of Energy, Office of Science, Office of Basic Energy Sciences under contract no. DE-FG02-04ER15614 for support. J.K. and K.K. acknowledge support from the Cluster of Excellence "Advanced Imaging of Matter" of the Deutsche Forschungsgemeinschaft (DFG), EXC 2056, project ID 390715994. J.K. and R.A.L. thank the Cluster of Excellence "Center for Ultrafast Imaging" (CUI, EXC 1074, ID 194651731) of the Deutsche Forschungsgemeinschaft for support. J.K. and K.K. acknowledge support from Deutsches Elektronen-Synchrotron DESY, a member of the Helmholtz Association (HGF). L.F.D. thanks the US National Science Foundation under contract no. 1605042 for support. T.P. acknowledges support by the Deutsche Forschungsgemeinschaft (DFG, German Research Foundation) under Germany's Excellence Strategy EXC2181/1-390900948 (the Heidelberg STRUCTURES Excellence Cluster). All authors acknowledge support of the US Department of Energy, Office of Science, Office of Basic Energy Sciences under contract no. DE-AC02-76SF00515. **Author contributions:** The experiment was carried out by K.S., S.A., G.S., A.R., R.O., A.A., N.B., C.B., G.C., R.C., P.H., Y.I., K.K., Y.K., J.K., Y.H.L., H.L., R.A.L., S.M., K.M., K.N., T.O., D.Ra., D.Ro., S.T., F.T., K.U., J.U., J.Z., C.P.S., and T.P. Theory work was performed by U.S., J.M.R., R.S., M.C.-G., G.P., and F.R. The original draft was prepared by K.S., S.A., U.S., F.R., C.P.S., and T.P. The manuscript was reviewed and edited by all authors. **Competing interests:** The authors declare that they have no competing interests. **Data and materials availability:** All data needed to evaluate the conclusions in the paper are present in the paper and/or the Supplementary Materials.

Submitted 22 May 2025
Accepted 20 October 2025
Published 21 November 2025
10.1126/sciadv.adz1900

Supplementary Materials

Experimental setup

Soft X-ray pulses with a central photon energy of 1.8 keV at a repetition rate of 120 Hz were generated by the Linac Coherent Light Source (LCLS) (*37*) at the Stanford Linear Accelerator Center (SLAC). Based on electron-bunch length measurements, the X-ray pulse duration was estimated to be 30 fs (FWHM). The C_{60} pump-probe experiments were performed at the AMO (Atomic, Molecular and Optical science) endstation (*40*) using the LAMP instrument (*38*) configured in scattering geometry with a pair of pnCCD detectors (*41*) ($78\times74\,\mathrm{mm}^2$ full area, 75×75 µm pixel size, 3.2 cm gap) at a distance of 7 cm downstream of the interaction point. Using a pair of KB mirrors, the soft X-ray pulses were focused to a diameter of ∼20 µm (FWHM) reaching intensities of $\sim10^{16}\,\frac{\mathrm{W}}{\mathrm{cm}^2}$ in the interaction point assuming 20 % beamline transmission. Optical laser pulses with 800 nm central wavelength, 3 mJ pulse energy and ∼30 fs (FWHM) pulse duration were generated by the AMO Ti:sapphire laser system (*42*). The optical laser pulses were focused using an out-of-vacuum lens with a focal length of 1 m to a diameter of ∼60 µm (FWHM) and collinearly overlapped with the X-rays using an in-vacuum incoupling mirror mounted under 45° with a central hole allowing the X-rays to pass through. Spatial overlap of the NIR and X-ray beams was ensured by monitoring them on a frosted YAG crystal mounted on a diagnostics paddle that was inserted in the interaction point before and in between the pump-probe measurements. The NIR intensity was scanned between $2\times10^{13}\,\frac{\mathrm{W}}{\mathrm{cm}^2}$ and $8\times10^{14}\,\frac{\mathrm{W}}{\mathrm{cm}^2}$ using a polarizer–waveplate combination.

Both, the optical and X-ray beam were focused into a beam of gas-phase C_{60} molecules, generated by an oven resistively heated to 870 K (*43*). C_{60} powder (purchased from Sigma Aldrich with 99.9 % purity) was evaporated through a conically shaped copper tip with a 1 mm hole diameter reaching a target density of roughly $10^{11}\,\frac{\mathrm{particles}}{\mathrm{cm}^3}$ in the interaction point, located 5 mm below the tip. Simultaneous operation of the hot oven and the cryogenically cooled (−50 °C) pnCCD detectors was achieved by means of a three-layer heat shield around the oven.

Scattering images of an ensemble of C_{60} molecules were recorded with the pnCCD detectors. In addition, time-of-flight (TOF) spectra were recorded alternating with the scattering measurements using a compact TOF spectrometer (*44, 45*). Details of the experimental setup are shown in Fig. S1.

The ion TOF spectrometer was designed with the purpose to serve as a compact detector for measuring charge state distributions to be used in combination with a large area scattering detector (*44*). As shown in Fig. S1, the TOF spectrometer was mounted on a linear stage to be able to retract it from the interaction region for operation with the pnCCD detector close to the oven and the catcher placed over the oven. Figure S1 shows the experimental setup in TOF configuration with the spectrometer in position for recording TOF spectra. The TOF spectrometer consists of a repeller and extractor

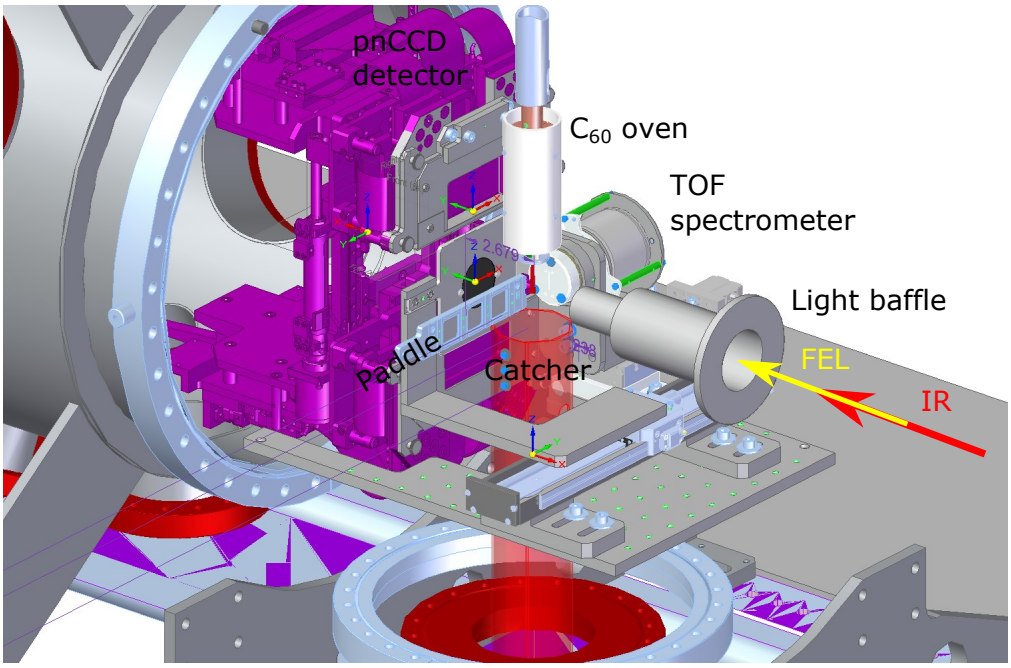

Figure S1: **Layout of the experimental setup.** The FEL and NIR beam arrive from the lower right, pass through a light baffle to suppress background scattering and interact with C_{60} molecules injected by the resistively heated oven from the top. The oven is mounted on a xyz-manipulator for fine adjustment. Scattered photons are detected by the pnCCD detector in the back and the FEL and NIR beam pass through the adjustable central gap of the two detector halves. The C_{60} molecular beam is dumped into a catcher, which is mounted on a xyzϕ-manipulator from the bottom to be able to completely cover the oven during operation of the cooled pnCCD detector. Alternatively – with the catcher lowered, as shown here – TOF spectra can be recorded with a compact TOF spectrometer, which is mounted on a linear translation stage to drive it into the interaction point. In this mode, the cooled pnCCDs are retracted to the back. Instead of the TOF spectrometer, a diagnostics paddle with a clear and a frosted YAG screen and a SMA "antenna" for establishing rough spatial and temporal overlap can be inserted into the interaction region.

electrode, with a separation of 40 mm between each other and the FEL passing through the center between the electrodes. The repeller was grounded and mounted on the diagnostics paddle while the extractor was kept at a potential of −900 V. The entrance to the 40 mm drift region was sealed off with a 1 mm width vertical slit and terminated with a mesh before the MCP. The TOF signal was detected with a commercial MCP/scintillator/photo multiplier combination (Photonis Bipolar TOF, APD BPTOF 25/6/5/12 D 60:1 MP EDR), as detailed in Ref. (*45*), and acquired with a commercial Aquiris digitizer. The front of the MCP facing the interaction region was supplied with a voltage of −2150 V, the back of the MCP with −1000 V, the scintillator with 2050 V and the photo multiplier with −800 V. Please note that for an ion kinetic energy of roughly 1 keV the detection efficiency for small fragments is larger than for large fragments (*28*).The polarization of both the FEL and the NIR beams was horizontal in the plane of the TOF spectrometer.

Experimental procedures

NIR-pump–X-ray-probe spectra were recorded over a delay range of ±1 ps, where positive delays denote a preceding NIR pulse and negative delays preceding X-rays. The delay of the NIR pulse was continuously scanned during the measurement with a step size of 10 fs. For each NIR intensity, scans of 20 minutes were recorded and repeated multiple times. For each shot, the jitter between the NIR and X-ray pulses was characterized with a time tool based on the spectral encoding technique (*46*). Long-term timing drifts were measured and corrected every few hours by repeating a delay scan at the highest NIR intensity and monitoring the position of the sharp drop in scattering intensity due to disintegration of the C_{60} molecules (cf. Fig. 2d). The spatial overlap of the NIR and the X-ray beam was fine tuned using the same signal, however at lower NIR intensities to avoid saturation effects.

The temporal overlap of the NIR and FEL pulses (referred to as time zero t_0) in the interaction point was determined in a separate delay-dependent TOF measurement on N_2 molecules. The method was previously applied and is described in detail in Ref. (*47*). Briefly, the yield of N_2^{2+} ions divided by the yield of N^{2+} ions, plotted as a function of the pump-probe delay, results in a step-function that indicates t_0 (cf. Fig. S2). The signal originates from N_2^{2+} ions, produced by the absorption of one X-ray photon, which are dissociated by the NIR laser once it arrives later than the X-rays, resulting in a depleted number of bound dications and an increased number of N^{2+} ions. Each shot is jitter-corrected with the time-tool information. In order to determine time zero, the delay-dependent step function is fitted with a generalized error function

$$e(t) = a \cdot \mathrm{erf}\left(\frac{t - t_0}{\sigma}\right) + c \tag{5}$$

with the fit parameters: amplitude a, constant offset c, t_0, and σ, where FWHM $= 2 \cdot \sqrt{\ln 2} \cdot \sigma$ corresponds to the instrument response function. Multiple scans were repeated,

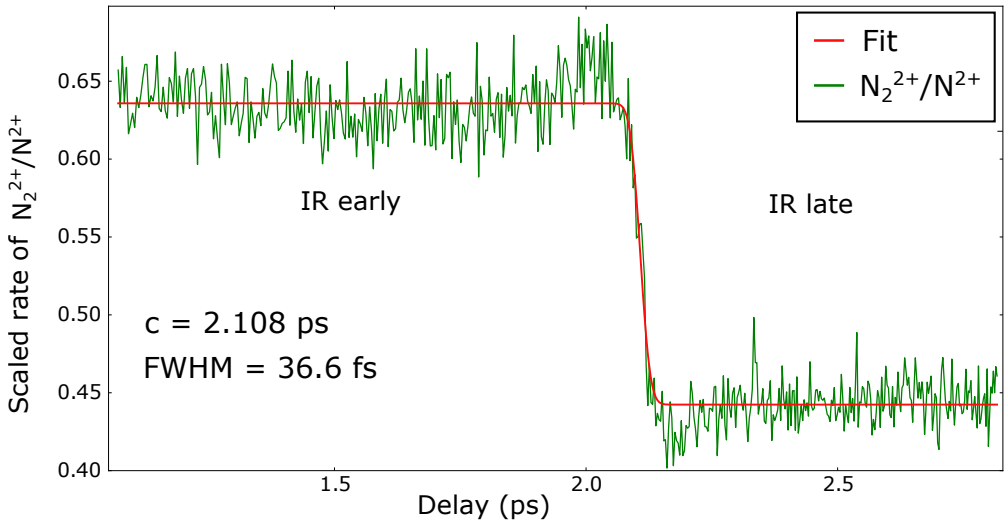

Figure S2: **Delay-dependent yield of molecular nitrogen dications N_2^{2+}, divided by the yield of dissociated N^{2+} ions.** The fit of the error function yields t_0 and an instrument response function of 37 fs (FWHM). The delays were jitter-corrected using a time tool.

yielding an instrument response function of 38 ± 3 fs (FWHM).

Detector calibration

The scattering detector calibration was performed in four steps, as illustrated in Fig. S3. The raw image, shown in Fig. S3a, contains all detected photons. The photon-energy distribution in analog-to-digital units (ADU) is shown in Fig. S3e. A cut-out around the photon energy of 1.8 keV of elastically scattered photons is applied, resulting in Fig. S3b. The same energy range was used for all recorded data. Some malfunctioning areas on the detector require a gain correction which was performed by scaling the gain in these areas to match the gain to the rest of the detector, as illustrated in Fig. S3f,g. A gain-corrected detector image is shown in Fig. S3c. Since the gain was slowly drifting over time, the gain correction was repeated for every scan. Furthermore, all images contain background scattering from beamline components, which was minimized in every shift but could not be completely avoided. A new background image without the NIR laser and no target, such as Fig. S3h, was recorded at the beginning of each shift after beamline stray light optimization and subtracted from the gain corrected detector image for each scan.

We detected on average 120 scattered photons per shot, with ∼10 of these photons stemming from background.

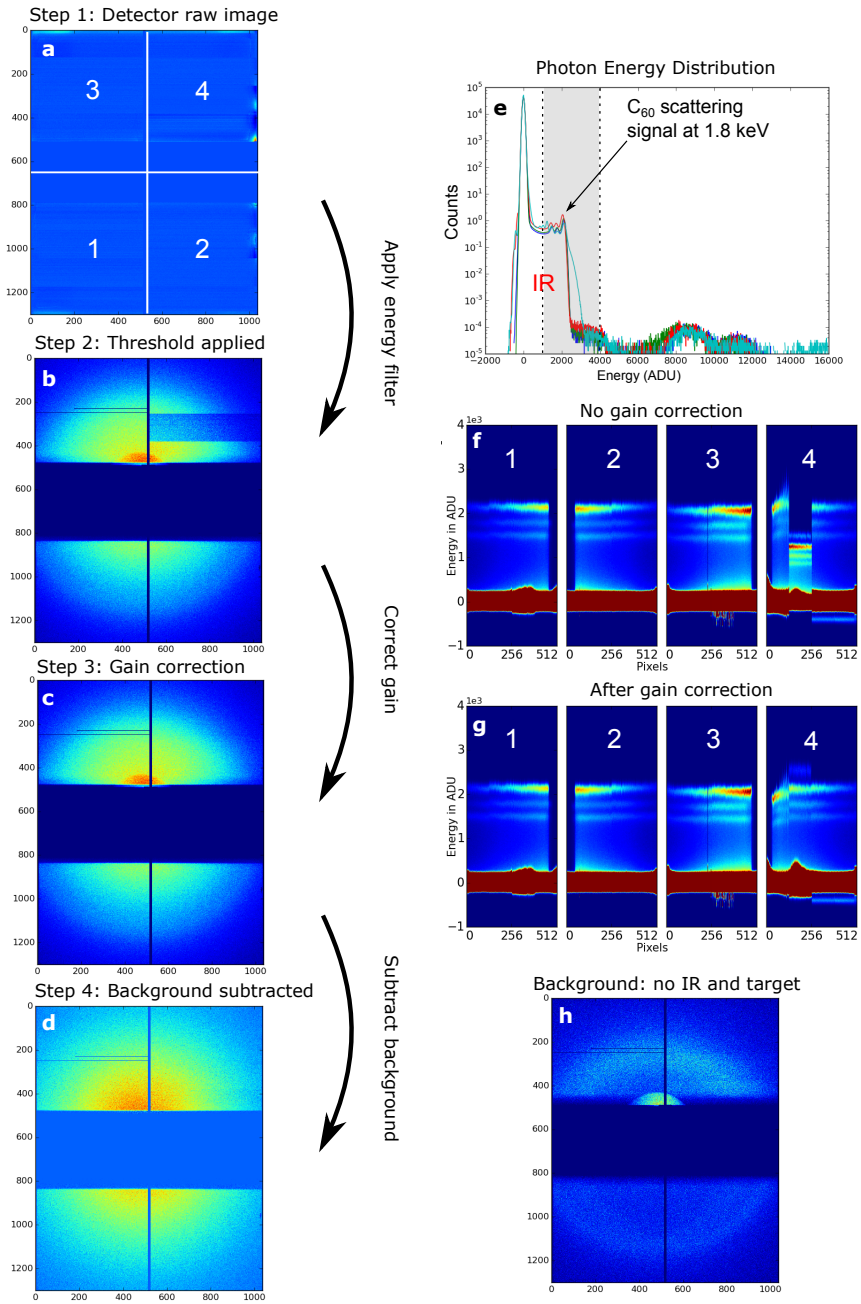

Figure S3: **Applied sequence of detector calibration steps.** (**a**) raw detector image, sectors are labeled with numbers 1–4; (**b**) detector image of selected photons with energies around the elastic scattering photon energy, shown in (**e**); (**c**) detector image after gain correction of sector 4, comparison before and after shown in (**f**) and (**g**) respectively; (**d**) detector image after background subtraction; (**h**) background recorded with no optical laser and without target.

Guinier fit

In order to relate the changes in the widths of the scattering images with the structural changes of the C_{60} molecules, we perform Guinier fits on the recorded images (following the description in Sec. 2.1.2.6 of Ref. (*27*)). We extract the normalization of the delay-dependent radii (cf. Fig. 2e-h) from Guinier fits to static X-ray diffraction data, i.e., from unperturbed C_{60} molecules.

The scattering intensity $I(q, R)$ for a spherical object is given by:

$$I(q, R) = I_\mathrm{e}(q)\, F^2(q, R), \tag{6}$$

$$F(q, R) \stackrel{!}{=} F_\mathrm{Guinier}(q, R) = \underbrace{V_\mathrm{sph}(R)\, \rho_\mathrm{e}}_{N} \left(3\, \frac{\sin(qR) - qR\, \cos(qR)}{(qR)^3} \right), \tag{7}$$

where $q = 4\pi \sin(\theta/2)/\lambda$ is the momentum transfer, θ the scattering angle, λ the wavelength, R the radius of the sphere, $I_\mathrm{e}(q)$ the intensity scattered by a free electron, $V_\mathrm{sph}(R) = \frac{4}{3}\pi R^3$ the volume of the target, and $\rho_\mathrm{e} = \frac{N}{V_\mathrm{sph}(R)}$ the average electronic scatterer density with N being the number of scatterers.

For an ellipsoidal target, R is replaced by

$$r(R_\mathrm{pol}, R_\mathrm{equ}, \theta) = \sqrt{R_\mathrm{equ}^2\, \sin^2\theta + R_\mathrm{pol}^2\, \cos^2\theta} \tag{8}$$

and the volume $V_\mathrm{sph}(R)$ becomes $V_\mathrm{elip}(R_\mathrm{pol}, R_\mathrm{equ}) = \frac{4}{3}\pi\, R_\mathrm{pol}\, R_\mathrm{equ}^2$.

For the fit of the scattering images, we added a constant background and re-arranged the function to

$$I(q, R_\mathrm{pol}, R_\mathrm{equ}) = A(q, R_\mathrm{pol}, R_\mathrm{equ}) \left(3\, \frac{\sin(qR) - qR\, \cos(qR)}{(qR)^3} \right)^2 + \mathrm{const}, \tag{9}$$

$$A(q, R_\mathrm{pol}, R_\mathrm{equ}) = I_\mathrm{e}(q)\, V_\mathrm{elip}^2(R_\mathrm{pol}, R_\mathrm{equ})\, \rho_\mathrm{e}^2 = I_\mathrm{e}(q) N^2, \tag{10}$$

with $R = r(R_\mathrm{pol}, R_\mathrm{equ}, \theta)$ as in Eq. 8. $I_\mathrm{e}(q)$ is assumed to be constant in θ. Thus, $A(q, R_\mathrm{pol}, R_\mathrm{equ})$ becomes $A(R_\mathrm{pol}, R_\mathrm{equ})$, i.e., independent of θ. As A is now only dependent on fit parameters, it can simply be a constant fit parameter for the whole detector plane. Since A is proportional to the number of scatterers squared, it is a measure of the degree of fragmentation and ionization of the C_{60} molecules.

In the calculation of the fit function, we take the detector shape into account. Specifically, we calculate an intensity for each 3D pixel position, hence this includes the $\cos^3\theta$ distortion.

Figure S4 shows the detector images from Fig. 1 and illustrates the performance of the Guinier fit. Four different delay ranges at the intermediate NIR intensity are selected to showcase different scattering scenarios:

- delay < 0 fs: intact molecules with highest photon yield. The C_{60} ground-state radii in Fig. 2 and Fig. 4 are normalized to the mean of the fitted Guinier radius for negative delays.
- delay ~ 0 fs: expanding molecules with slightly reduced photon yield
- delay > 0 fs: Coulomb-exploding molecules with clearly reduced photon yield
- delay $\gg 0$ fs: disintegrated molecules with lowest photon yield

The panels in Fig. S4 are grouped according to the four aforementioned delay ranges. Each subfigure (a) shows the experimental raw detector image with 4×4 pixels binned together. The corresponding ellipsoidal Guinier fit results with detector mask are shown in subfigures (b). Please note that reported Guinier fit results always stem from ellipsoidal Guinier fits. The projections on the y-axis of subfigures (a) and (b) are shown in blue and orange respectively in subfigures (c). The results of the Guinier fits without detector mask are shown in subfigures (d). The raw detector images with gaps filled from the fit are shown in subfigures (e). The projections on the y-axis of subfigures (d) and (e) are shown in orange and blue respectively in subfigures (f). The ensemble-averaged Guinier radii shown in Fig. 2 and Fig. 4 correspond to the fit results from the y-projection. The y-direction was chosen because the detector covers a larger area. The fit results in x-direction agree within error bars.

Relation between Guinier amplitude and molecular fragmentation

The Guinier amplitude is proportional to the squared number of scatterers in each moiety (N^2), as shown in Eq. 10. We denote the number of scatterers for an intact C_{60} molecule as N_0. If we assume a break-up into m equally large fragments with $N_m = \frac{N_0}{m}$, the ratio of Guinier amplitudes A_0 for an intact molecule and A_m for m fragments is

$$\frac{A_0}{A_m} = \frac{N_0^2}{\sum_{i=1}^{m} N_i^2} = \frac{N_0^2}{m\left(\frac{N_0}{m}\right)^2} = m. \tag{11}$$

Thus, the Guinier amplitude decreases linearly with the number of fragments under the assumption that fragments are (roughly) equally large. For very asymmetric break-up into a large moiety and small fragments, the Guinier amplitude drops slower with the number of fragments because the term N_{large}^2 for a large fragment dominates the denumerator.

For the direct removal of k electrons from a structural intact C_{60} molecule through photoionization by the NIR laser, the Guinier amplitude drops to $(N_0 - k)^2$.

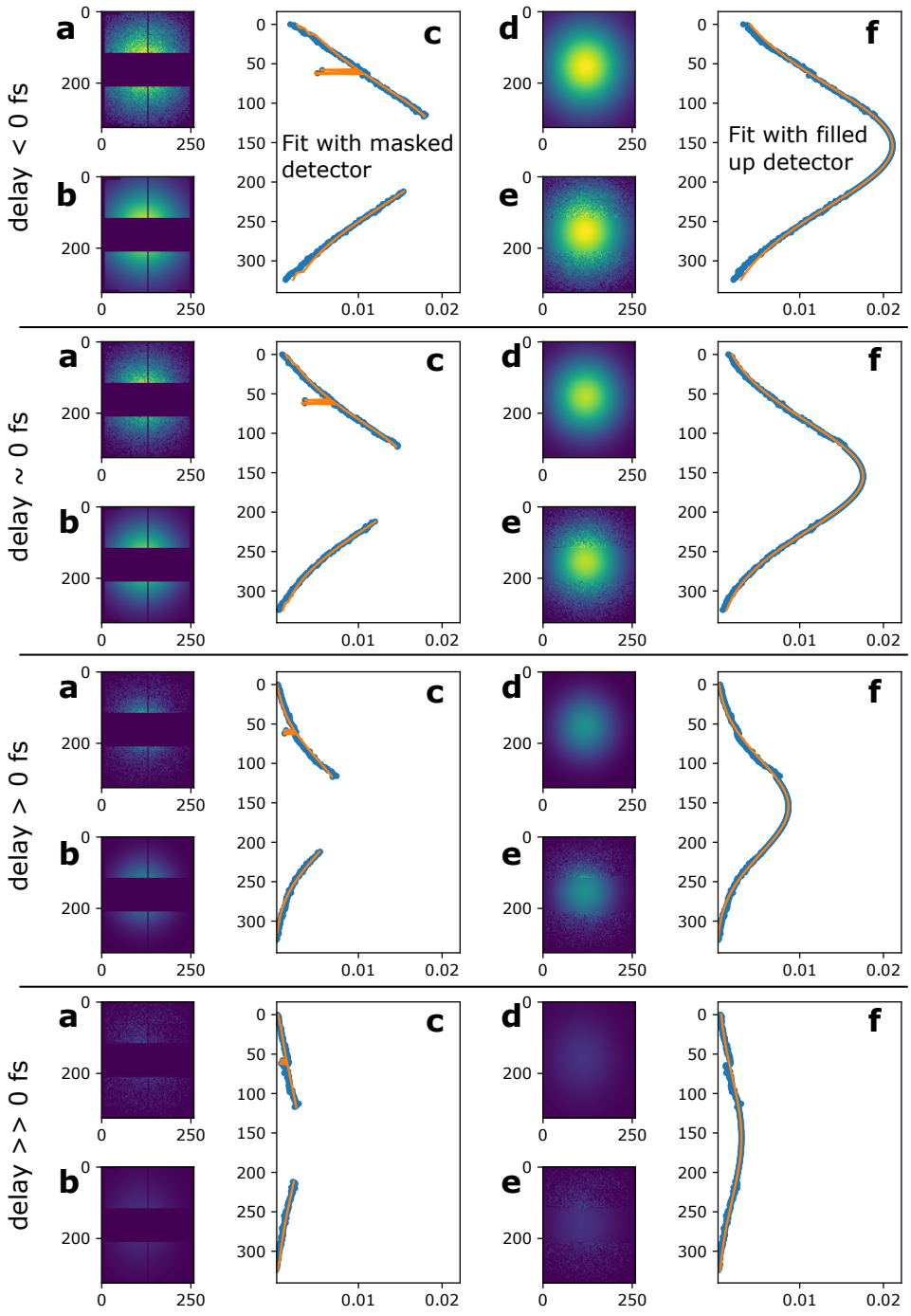

Figure S4: **Ellipsoidal Guinier fits at the intermediate NIR intensity for four different delays (from top to bottom), grouped in panels respectively.** **a**, raw detector image with 4×4 pixel binning; **b**, fit result with detector mask; **c**, projections on y axis of (**a**) in blue and (**b**) in orange; **d**, fit result without mask; **e**, image (**a**) with gaps filled from fit and **f**, projections on y axis of (**d**) in orange and (**e**) in blue.

Uncertainty estimation

The error bands in Fig. 2 are calculated by selecting the first 350 fs (35 bins × 10 fs) of each delay scan and determining the standard deviation thereof. Since these delays lie in the negative range before the molecules show any dynamical response, the fluctuations represent the noise of the data.

Fitting procedures

The fitting procedure to extract time scales for the dynamics of the ensemble-averaged radius at the intermediate intensity are illustrated in Fig. S5. The expansion dynamics, represented by the rising edge in Fig. S5 is fitted with an error function $r(t)$. The decay of the radius is fitted with an exponential decay function $d(t)$. The complete fitting function is the product of $r(t)$ and $d(t)$, convoluted with a Gaussian function with a width corresponding to the instrument response function. The fit yields a rise time of 140 ± 5 fs (FWHM) and an exponential decay time $\tau = 155 \pm 10$ fs.

$$r(t) = \mathrm{erf}\Big(\frac{t - t_0}{\sigma}\Big) \tag{12}$$

with FWHM $= 2 \cdot \sqrt{\ln 2} \cdot \sigma$

$$d(t) = \exp\Big(-\frac{t - t_0}{\tau}\Big) + c \tag{13}$$

Figure 3a shows the decrease of the delay-dependent scattering amplitudes for different IR intensities. For each IR intensity, multiple delay scans were recorded and each of them fitted with an error function (cf. Eq. 7). The plotted data points represent the averaged fitted FWHM of the scattering amplitude steps, as shown for the low, intermediate and high NIR intensity and a single data set in Fig. 2b-d. The given error bars represent the standard error.

Influence of X-ray pulses

We neglect perturbation by the X-rays (i.e., ionization and break-up induced thereof within the X-ray pulse duration) in the experimental interpretation and do not include the interaction of the probe pulse into the simulations. This assumption is based on the results of previous work which has explicitly studied the response of C_{60} to intense XFEL pulses. Both, the fragmentation of C_{60} in single intense XFEL pulses (*48*) and the X-ray induced evolution of the break-up was studied using an X-ray pump-probe scheme (*12*). The latter publication comes to the conclusion that the atomic displacement for up to 30 fs after the peak of the X-ray pulse does not exceed 2 Å. We have compared the pulse parameters reported in Ref. (*12*) with the current study and conclude that the amount

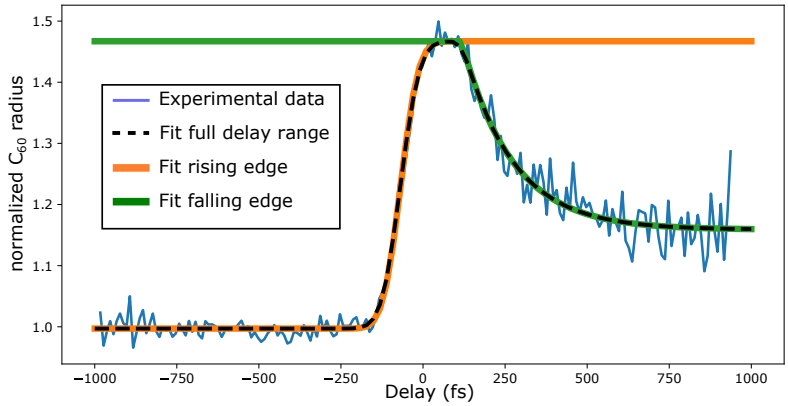

Figure S5: **Fit procedure for Fig. 2g.** The experimental data (blue solid line) is shown together with the fit over the full delay range (black dashed line). The fit function takes into account the rising edge, which is fitted with an error function (solid orange line), the falling edge, which is fitted with an exponential decay (solid green line), and both folded with a Gaussian function representing the instrument response function. The fit yields a rise time of 140 ± 5 fs (FWHM) of the error function and an exponential decay time $\tau = 155 \pm 10$ fs.

of photons absorbed per molecule should be about a factor of 3 lower in the present experiment. Thus, the displacement of the atoms within our 30 fs pulses can be safely neglected. Based on Ref. (*48*), we can estimate the average amount of absorbed X-ray photons per pulse to about 5, which should result in a loss of in average less than 10 electrons over the pulse from photoionization and Auger-Meitner decay. The effect on the scattering cross section (5 parts in 360) is therefore minor.

Theory

Classical molecular dynamics simulations

The process of laser strong-field excited/ionized C_{60} molecules is calculated by means of classical molecular dynamics (MD) similar to the ones applied to clusters (*49*) and fullerenes (*12*) previously. This is justified by the fact that at these rather high intensities of the NIR laser pulses low-lying electronic states do not play a role but many highly-excited electrons are created. This situation can be considered as a nano-plasma. Important processes like electron-ion or electron-electron collisions or electron transfer (hopping) are all contained in the description, albeit on a classical level. A (TD)DFT description is not only out of reach since (i) we have to treat simultaneously many electrons bound to the C_{60} atoms as well as continuum electrons quivering in the laser field over large distances, and (ii) we have to perform a proper focal averaging over many intensities.

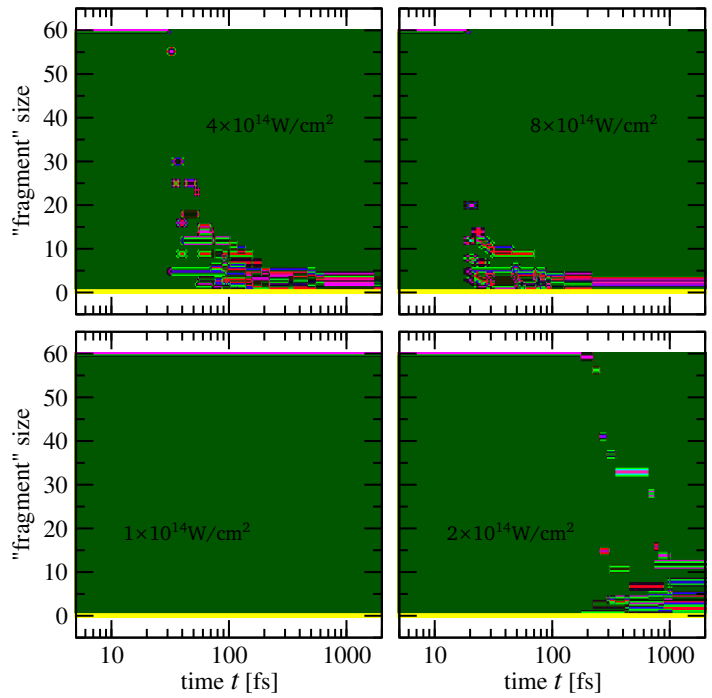

Figure S6: **Time-dependent fragment-size distribution of C_{60} for four different laser intensities, calculated using our classical dynamics simulations.** The peak of the NIR pulse is at time $t = 0\,\mathrm{fs}$.

It would also completely fail to account for electron-electron collisions, which are crucial in a dense, quickly thermalizing nano-plasma like this.

Our calculations are based on standard empirical short-range two- and three-body forces (*39*) developed for the description of systems with covalent bonds. As a test, we have reproduced melting calculations (*50*), which were based on different forces. The initial temperature of the C_{60} in the simulations was set to 800 K.

A new feature of our simulation is the inclusion of pairwise Coulomb interactions between electrons and carbon ions, which is required to account for (multiple) ionization of C_{60}. Therewith the equations of motions read

$$\ddot{\mathbf{r}}_j = \sum_{j' \neq j} \mathbf{f}_\alpha(\mathbf{r}_j, \mathbf{r}_{j'}) - \sum_J \mathbf{f}_\alpha(\mathbf{r}_j, \mathbf{R}_J) - \mathcal{E}(t) \tag{14a}$$

$$M\ddot{\mathbf{R}}_J = \sum_{J' \neq J} \mathbf{f}_\alpha(\mathbf{R}_J, \mathbf{R}_{J'}) - \sum_j \mathbf{f}_\alpha(\mathbf{R}_{\{J'\}}, \mathbf{r}_j) + \mathbf{F}_J(\mathbf{R}_J) + \mathcal{E}(t) \tag{14b}$$

$$\mathbf{f}_\alpha(\mathbf{x}, \mathbf{y}) \equiv \frac{\mathbf{x} - \mathbf{y}}{|[\mathbf{x} - \mathbf{y}]^2 + \alpha^2|^{3/2}} \tag{14c}$$

$$\mathcal{E}(t) \equiv \mathbf{e}_z \, \mathrm{e}^{-2\ln 2\, t^2/T^2} \sin(\omega t), \tag{14d}$$

with capital (M, $\mathbf{R}$, J) and small ($\mathbf{r}$, j) letters denoting ions and electrons, respectively. We treat one electron per atom, i. e. all indices run from 1 to 60. The Coulomb interaction $\mathbf{f}_\alpha$ is smoothed in order to prevent artificial auto-ionization as it is done routinely in MD calculations of laser-cluster interactions (*49*). We have chosen as smoothing parameter $\alpha = 3.58\,\mathrm{a_0}$, which guarantees that the ionization potential $\mathrm{IP}_{\mathrm{C_{60}}} = 7.6\,\mathrm{eV}$ is correctly reproduced. We use the standard expression for the Tersoff force $\mathbf{F}_J$ (*39*). We do not adjust the Tersoff force when the C_{60} becomes charged. The driving laser pulse $\mathcal{E}(t)$ has a Gaussian envelope with a FWHM duration T and the laser frequency ω defined by the wavelength $\lambda = 800\,\mathrm{nm}$. The low number of particles does not require any sophisticated propagation scheme.

We follow the positions of all electron and ions over time according to the Eqs. (14) and calculate scattering images with

$$P_\delta(k_x, k_y) = \int \mathrm{d}t\, \mathrm{e}^{-4\ln 2\,[t-\delta_\mathrm{x}]^2/T_\mathrm{x}^2} \left| p(k) \sum\nolimits_J \mathrm{e}^{\mathrm{i}\mathbf{k}\cdot\mathbf{R}_J(t)} \right|^2 \tag{15a}$$

$$\mathbf{k} = \{k_x, k_y, 0\}, \qquad k = |\mathbf{k}|, \tag{15b}$$

with the atomic structure factor $p(k)$, which is not altered for charged C_{60}. Note that we average in Eq. (15a) over the time t weighted with a Gaussian representing the X-ray pulse with a FWHM of T_x and a delay with respect to the driving NIR laser of δ_x. The time-dependent fragment-size distribution is plotted in Fig. S6. Notably, the break-up into smaller fragments accelerates with the laser intensity, which is in line with the experimental findings.

Additional heating

The calculation presented above does not reproduce the abrupt crossover from long-term stability to direct fragmentation, as observed in the experiment. One possible reason might be that the strong NIR pulse interacts with the core electrons leading to additional heating of the C_{60} backbone (*11*). To account for this heating we use a simple ad-hoc term in our calculation: In each time step all carbon atoms are kicked along their instantaneous velocity. The total intensity-dependent heating energy is defined as $\Gamma(t) = \frac{I(t)}{10^{14}\mathrm{W/cm^2}}\Gamma_0$ with $I(t)$ the instantaneous intensity and $\Gamma_0 = 40\,\mathrm{eV/fs}$. Figure S7 shows the result of the this calculation where one sees indeed an abrupt unset of the increase of the C_{60} radius indicating the onset of fragmentation.

Quantum dynamics simulations

In the quantum dynamics simulations, the neutral ground state (GS) of C_{60} is photoexcited and photoionized with a few-cycle NIR pulse centered at t_0, with a wavelength of $\lambda = 720\,\mathrm{nm}$ ($\omega = \frac{2\pi v}{\lambda}$) and a CEP $\phi = 0$. The peak intensity is $5.6 \times 10^{13}\,\frac{\mathrm{W}}{\mathrm{cm^2}}$, which gives a maximum electric field E_0 of 0.04 au. The pulse is linearly polarized in the y direction,

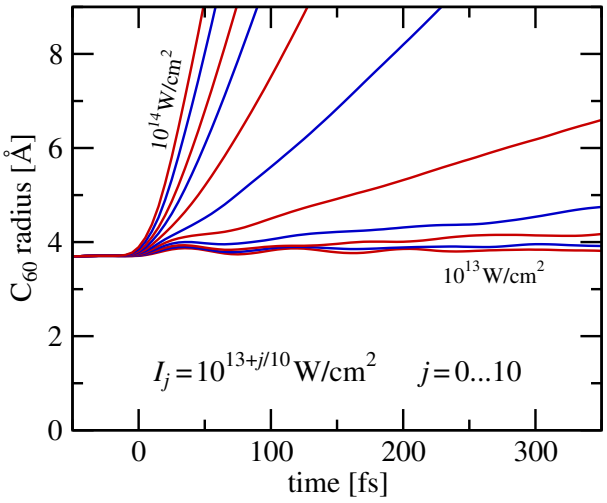

Figure S7: **Effect of the intensity-dependent heating.** The radius of C_{60} is shown as a function of time t for various intensities I_j specified in the figure. The plotted radius is defined as $R(t) = \frac{1}{60}\sum_{A=1}^{60}|\mathbf{R}_A(t)|$ with $\mathbf{R}_A(t)$ being the position of atom A in the center-of-mass frame at time t as obtained with the MD calculation.

$\boldsymbol{e} = \boldsymbol{e}_y$. The analytical form of the time profile of the electric field is derived from the derivative of the vector potential $\boldsymbol{A}(t)$, $\boldsymbol{E}(t) = -\frac{d\boldsymbol{A}(t)}{dt}$ to ensure that there is no source term (*51*):

$$\boldsymbol{E}(t) = \boldsymbol{e}\, E_0 \exp\left(\frac{-(t-t_0)^2}{2\sigma^2}\right)\left[\cos(\omega t+\phi) - \frac{2(t-t_0)\sin(\omega t+\phi)}{\omega\sigma^2}\right] \qquad (16)$$

$\boldsymbol{A}(t)$ has a Gaussian envelope with a σ of 1.36 fs, (FWHM $= 2\sqrt{2\ln 2}\sigma = 3.2$ fs). The time-dependent Schrödinger equation (TDSE), $i\hbar\frac{d\psi(t)}{dt} = H(t)\psi(t)$, is solved for the electronic wave function $\psi(t)$ at the equilibrium geometry of the neutral GS. The initial state, $\psi(0)$, is the ground electronic state. The coupling with the electric field that leads to photoexcitation and photoionization is included explicitly in the electronic Hamiltonian in the dipole approximation, $\boldsymbol{H}(t) = \boldsymbol{H}_0^{\text{elec}}(\boldsymbol{r}) - \boldsymbol{E}(t)\cdot\boldsymbol{\mu}$, where $\boldsymbol{r}$ stands for the electronic coordinates and $\boldsymbol{\mu}$ is the electronic dipole operator. The TDSE is solved using a coupled-equation scheme as described in Refs. (*52*) and (*53*) based on the partitioning technique in a bound subspace **Q** and an ionized subspace **P**. The ground state and 406 excited states converging to the ionization potential are included in the bound subspace **Q**. The electronic structure of the 500 lowest excited states of C_{60} has been computed in TD-DFT with the long range corrected CAM-B3LYP functional (*54*) and a 6-31+G(d) basis set augmented by 6 s, p and d additional diffuse functions centered in the middle of the C_{60} cage (*55*). Very diffuse basis functions were added in order to describe the highly excited Rydberg and SAMO (Super-Atom-Molecular-Orbitals) states below the ionization potential (IP). The ionized subspace **P** is spanned on a basis of ionized states built from

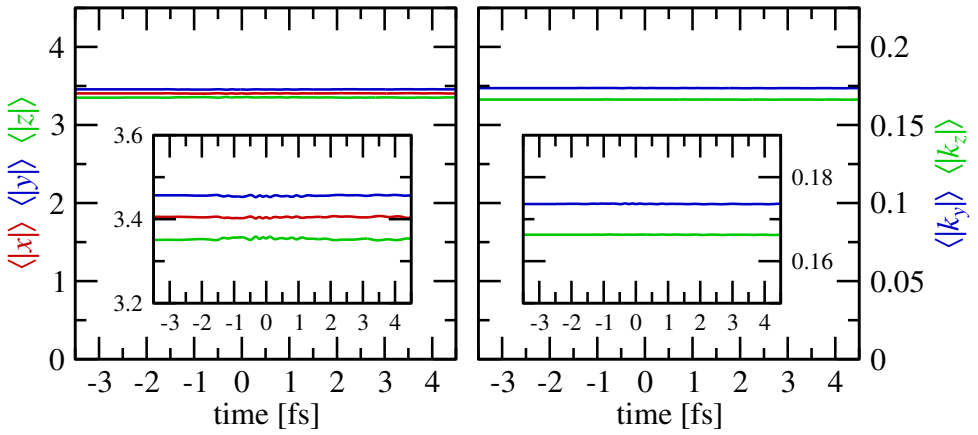

Figure S8: **Delay-dependent scattering signal extracted from quantum calculations.** The average absolute values of x, y and z of the electron density is shown in the left panel. The k_y- and k_z-components in the detector plane are shown in the right panel.

the antisymmetrized product of the field-free ground state of the cation Ψ_{cat} and the wavefunction of the ionized electron χ_k which is an orthogonalized plane wave (*56, 57*) with a wave vector $\mathbf{k}$. The ground state of the cation is five times degenerate. For each cationic state, an ionization continuum discretized in energy and angle is associated. The momentum of the ionized electron varies between 0 and 2 au with a stepsize of 0.01 au and a set of 80 solid angle values is associated to each momentum value. Therefore, the ionized subspace is spanned on a basis of 80'000 states.

The results obtained from the quantum calculations are shown in Fig. S8. The laser-induced modulation in the electron density under these intensity conditions are too small to be visible in scattering images. Longer laser pulses in this regime would further ionize the system and thus infringe the validity of using the 5 continua of a singly ionized C_{60} states, but massively blow up this hyper-continuum state space (exponentially with the number of ionized electrons). Intensities higher than $5.6 \times 10^{13}\,\frac{\text{W}}{\text{cm}^2}$ cannot currently be treated because they would require a prohibitive amount of states in the many-body continuum subspace. For intensities higher than $\sim 5 \times 10^{14}\,\frac{\text{W}}{\text{cm}^2}$, one would even need to go beyond the dipole approximation. The results using the $5.6 \times 10^{13}\,\frac{\text{W}}{\text{cm}^2}$ field strength factually prove that the complex electronic dynamics arising with optical laser intensities higher than $5.6 \times 10^{13}\,\frac{\text{W}}{\text{cm}^2}$ cannot be captured by fully quantum calculations.

Supplemental movies

We provide movies of the classical MD simulations for the four NIR intensities displayed in Fig. 4. They show the scattering images of a single C_{60} molecule (left) with the dynamics of the corresponding molecule (middle) and the ensemble averaged scattering pattern

(right). The following four files for perturbative, low, intermediate and high intensities, respectively, are available as supplemental movies:

Caption for i2.0e13-l800-d45-dx25.mp4: Movie 1 "Perturbative Intensity Regime" – Time-dependent response and scattering images of laser-excited single (left) and ensemble-averaged (right) C_{60} molecules at a laser intensity of $2 \times 10^{13} \frac{\mathrm{W}}{\mathrm{cm}^2}$.

Caption for i1.1e14-l800-d45-dx25.mp4: Movie 2 "Low Intensity Regime" – Time-dependent response and scattering images of laser-excited single (left) and ensemble-averaged (right) C_{60} molecules at a laser intensity of $1.1 \times 10^{14} \frac{\mathrm{W}}{\mathrm{cm}^2}$.

Caption for i2.5e14-l800-d45-dx25.mp4: Movie 3 "Intermediate Intensity Regime" – Time-dependent response and scattering images of laser-excited single (left) and ensemble-averaged (right) C_{60} molecules at a laser intensity of $2.5 \times 10^{14} \frac{\mathrm{W}}{\mathrm{cm}^2}$.

Caption for i8.0e14-l800-d45-dx25.mp4: Movie 4 "High Intensity Regime" – Time-dependent response and scattering images of laser-excited single (left) and ensemble-averaged (right) C_{60} molecules at a laser intensity of $8 \times 10^{14} \frac{\mathrm{W}}{\mathrm{cm}^2}$.

REFERENCES AND NOTES

1. A. D. Bandrauk, *Molecules in Laser Fields* (Springer Netherlands, Dordrecht, 1995), pp. 131–150.

2. B. J. Sussman, D. Townsend, M. Y. Ivanov, A. Stolow, Dynamic stark control of photochemical processes. *Science* **314**, 278 (2006).

3. P. H. Bucksbaum, A. Zavriyev, H. G. Muller, D. W. Schumacher, Softening of the H_2^+ molecular bond in intense laser fields. *Phys. Rev. Lett.* **64**, 1883 (1990).

4. L. J. Frasinski, J. H. Posthumus, J. Plumridge, K. Codling, P. F. Taday, A. J. Langley, Manipulation of bond hardening in H_2^+ by chirping of intense femtosecond laser pulses. *Phys. Rev. Lett.* **83**, 3625 (1999).

5. M. E. Corrales, J. González-Vázquez, G. Balerdi, I. R. Solá, R. de Nalda, L. Bañares, Control of ultrafast molecular photodissociation by laser-field-induced potentials. *Nat. Chem.* **6**, 785 (2014).

6. J. Kim, H. Tao, J. L. White, V. S. Petrović, T. J. Martinez, P. H. Bucksbaum, Control of 1,3-cyclohexadiene photoisomerization using light-induced conical intersections. *J. Phys. Chem. A* **116**, 2758–2763 (2012).

7. H. W. Kroto, J. R. Heath, S. C. O'Brien, R. F. Curl, R. E. Smalley, C_{60}: Buckminsterfullerene. *Nature* **318**, 162 EP (1985).

8. W. Krätschmer, L. D. Lamb, K. Fostiropoulos, D. R. Huffman, Solid C_{60}: A new form of carbon. *Nature* **347**, 354–358 (1990).

9. F. Lépine, Multiscale dynamics of C_{60} from attosecond to statistical physics. *J. Phys. B At. Mol. Opt. Phys.* **48**, 122002 (2015).

10. E. E. B. Campbell, K. Hansen, K. Hoffmann, G. Korn, M. Tchaplyguine, M. Wittmann, I. V. Hertel, From above threshold ionization to statistical electron emission: The laser pulse-duration dependence of C_{60} photoelectron spectra. *Phys. Rev. Lett.* **84**, 2128 (2000).

11. I. V. Hertel, T. Laarmann, C. P. Schulz, Ultrafast excitation, ionization, and fragmentation of C_{60}. *Adv. Atom. Mol. Optic. Phys.* **50**, 219–286 (2005).

12. N. Berrah, A. Sanchez-Gonzalez, Z. Jurek, R. Obaid, H. Xiong, R. J. Squibb, T. Osipov, A. Lutman, L. Fang, T. Barillot, J. D. Bozek, J. Cryan, T. J. A. Wolf, D. Rolles, R. Coffee, K. Schnorr, S. Augustin, H. Fukuzawa, K. Motomura, N. Niebuhr, L. J. Frasinski, R. Feifel, C. P. Schulz, K. Toyota, S. K. Son, K. Ueda, T. Pfeifer, J. P. Marangos, R. Santra, Femtosecond-resolved observation of the fragmentation of buckminsterfullerene following x-ray multiphoton ionization. *Nat. Phys.* **15**, 1279–1283 (2019).

13. G. P. Zhang, T. F. George, Controlling vibrational excitations in C_{60} by laser pulse durations. *Phys. Rev. Lett.* **93**, 147401 (2004).

14. M. Fischer, J. Handt, G. Seifert, R. Schmidt, Orientation dependence of energy absorption and relaxation dynamics of C_{60} in fs-laser pulses. *Phys. Rev. A* **88**, 061403 (2013).

15. V. R. Bhardwaj, P. B. Corkum, D. M. Rayner, Internal laser-induced dipole force at work in C_{60} molecule. *Phys. Rev. Lett.* **91**, 203004 (2003).

16. M. Boyle, T. Laarmann, I. Shchatsinin, C. P. Schulz, I. V. Hertel, Fragmentation dynamics of fullerenes in intense femtosecond-laser fields: Loss of small neutral fragments on a picosecond time scale. *J. Chem. Phys.* **122**, 181103 (2005).

17. T. Laarmann, I. Shchatsinin, A. Stalmashonak, M. Boyle, N. Zhavoronkov, J. Handt, R. Schmidt, C. P. Schulz, I. V. Hertel, Control of giant breathing motion in C_{60} with temporally shaped laser pulses. *Phys. Rev. Lett.* **98**, 058302 (2007).

18. H. O. Jeschke, M. E. Garcia, J. Alonso, Nonthermal fragmentation of C_{60}. *Chem. Phys. Lett.* **352**, 154–162 (2002).

19. S. L. Dexheimer, D. M. Mittleman, R.W. Schoenlein, W. Vareka, X.-D. Xiang, A. Zettl, C.V. Shank, "Ultrafast dynamics of solid C_{60}," in *Eighth International Conference on Ultrafast Phenomena*. Technical Digest Series (Optica Publishing Group, 1992).

20. K. Nakai, H. Kono, Y. Sato, N. Niitsu, R. Sahnoun, M. Tanaka, Y. Fujimura, Ab initio molecular dynamics and wavepacket dynamics of highly charged fullerene cations produced with intense near-infrared laser pulses. *Chem. Phys.* **338**, 127–134 (2007).

21. H. Fuest, Y. H. Lai, C. I. Blaga, K. Suzuki, J. Xu, P. Rupp, H. Li, P. Wnuk, P. Agostini, K. Yamazaki, M. Kanno, H. Kono, M. F. Kling, L. F. DiMauro, Diffractive imaging of C_{60} structural deformations induced by intense femtosecond midinfrared laser fields. *Phys. Rev. Lett.* **122**, 053002 (2019).

22. T. Gorkhover, S. Schorb, R. Coffee, M. Adolph, L. Foucar, D. Rupp, A. Aquila, J. D. Bozek, S. W. Epp, B. Erk, L. Gumprecht, L. Holmegaard, A. Hartmann, R. Hartmann, G. Hauser, P. Holl, A. Hömke, P. Johnsson, N. Kimmel, K.-U. Kühnel, M. Messerschmidt, C. Reich, A. Rouzée, B. Rudek, C. Schmidt, J. Schulz, H. Soltau, S. Stern, G. Weidenspointner, B. White, J. Küpper, L. Strüder, I. Schlichting, J. Ullrich, D. Rolles, A. Rudenko, T. Möller, C. Bostedt, Femtosecond and nanometre visualization of structural dynamics in superheated nanoparticles. *Nat. Photon.* **10**, 93–97 (2016).

23. M. P. Minitti, J. M. Budarz, A. Kirrander, J. S. Robinson, D. Ratner, T. J. Lane, D. Zhu, J. M. Glownia, M. Kozina, H. T. Lemke, M. Sikorski, Y. Feng, S. Nelson, K. Saita, B. Stankus, T. Northey, J. B. Hastings, P. M. Weber, Imaging molecular motion: Femtosecond x-ray scattering of an electrocyclic chemical reaction. *Phys. Rev. Lett.* **114**, 255501 (2015).

24. J. M. Glownia, A. Natan, J. P. Cryan, R. Hartsock, M. Kozina, M. P. Minitti, S. Nelson, J. Robinson, T. Sato, T. van Driel, G. Welch, C. Weninger, D. Zhu, P. H. Bucksbaum, Self-referenced coherent diffraction x-ray movie of ångstrom- and femtosecond-scale atomic motion. *Phys. Rev. Lett.* **117**, 153003 (2016).

25. K. Haldrup, G. Levi, E. Biasin, P. Vester, M. G. Laursen, F. Beyer, K. S. Kjær, T. Brandt van Driel, T. Harlang, A. O. Dohn, R. J. Hartsock, S. Nelson, J. M. Glownia, H. T. Lemke, M. Christensen, K. J. Gaffney, N. E. Henriksen, K. B. Møller, M. M. Nielsen, Ultrafast x-ray scattering measurements of coherent structural dynamics on the ground-state potential energy surface of a diplatinum molecule. *Phys. Rev. Lett.* **122**, 063001 (2019).

26. B. Stankus, H. Yong, N. Zotev, J. M. Ruddock, D. Bellshaw, T. J. Lane, M. Liang, S. Boutet, S. Carbajo, J. S. Robinson, W. du, N. Goff, Y. Chang, J. E. Koglin, M. P. Minitti, A. Kirrander, P. M. Weber, Ultrafast x-ray scattering reveals vibrational coherence following rydberg excitation. *Nat. Chem.* **11**, 716–721 (2019).

27. A. Guinier, G. Fournet, *Small-Angle Scattering of X-rays* (John Wiley & Sons, Inc., New York, 1st ed., 1955).

28. R. Ehlich, M. Westerburg, E. E. B. Campbell, Fragmentation of fullerenes in collisions with atomic and molecular targets. *J. Chem. Phys.* **104**, 1900–1911 (1996).

29. C. Rose-Petruck, K. J. Schafer, K. R. Wilson, C. P. J. Barty, Ultrafast electron dynamics and inner-shell ionization in laser driven clusters. *Phys. Rev. A* **55**, 1182–1190 (1997).

30. P. B. Corkum, Plasma perspective on strong field multiphoton ionization. *Phys. Rev. Lett.* **71**, 1994–1997 (1993).

31. J. Kou, V. Zhakhovskii, S. Sakabe, K. Nishihara, S. Shimizu, S. Kawato, M. Hashida, K. Shimizu, S. Bulanov, Y. Izawa, Y. Kato, N. Nakashima, Anisotropic coulomb explosion of C_{60} irradiated with a high-intensity femtosecond laser pulse. *J. Chem. Phys.* **112**, 5012–5020 (2000).

32. E. E. B. Campbell, R. D. Levine, Delayed ionization and fragmentation en route to thermionic emission: Statistics and dynamics. *Annu. Rev. Phys. Chem.* **51**, 65–98 (2000).

33. R. Boll, J. M. Schäfer, B. Richard, K. Fehre, G. Kastirke, Z. Jurek, M. S. Schöffler, M. M. Abdullah, N. Anders, T. M. Baumann, S. Eckart, B. Erk, A. de Fanis, R. Dörner, S. Grundmann, P. Grychtol, A. Hartung, M. Hofmann, M. Ilchen, L. Inhester, C. Janke, R. Jin, M. Kircher, K. Kubicek, M. Kunitski, X. Li, T. Mazza, S. Meister, N. Melzer, J. Montano, V. Music, G. Nalin, Y. Ovcharenko, C. Passow, A. Pier, N. Rennhack, J. Rist, D. E. Rivas, D. Rolles, I. Schlichting, L. P. H. Schmidt, P. Schmidt, J. Siebert, N. Strenger, D. Trabert, F. Trinter, I. Vela-Perez, R. Wagner, P. Walter, M. Weller, P. Ziolkowski, S. K. Son, A. Rudenko, M. Meyer, R. Santra, T. Jahnke, X-ray multiphoton-induced Coulomb explosion images complex single molecules. *Nat. Phys.* **18**, 423–428 (2022).

34. X. Li, R. Boll, P. Vindel-Zandbergen, J. González-Vázquez, D. E. Rivas, S. Bhattacharyya, K. Borne, K. Chen, A. de Fanis, B. Erk, R. Forbes, A. E. Green, M. Ilchen, B. Kaderiya, E. Kukk, H. V. S. Lam, T. Mazza, T. Mullins, B. Senfftleben, F. Trinter, S. Usenko, A. S. Venkatachalam, E. Wang, J. P. Cryan, M. Meyer, T. Jahnke, P. J. Ho, D. Rolles, A. Rudenko, Imaging a light-induced molecular elimination reaction with an X-ray free-electron laser. *Nat. Commun.* **16**, 7006 (2025).

35. B. Richard, R. Boll, S. Banerjee, J. M. Schäfer, Z. Jurek, G. Kastirke, K. Fehre, M. S. Schöffler, N. Anders, T. M. Baumann, S. Eckart, B. Erk, A. de Fanis, R. Dörner, S. Grundmann, P. Grychtol, M. Hofmann, M. Ilchen, M. Kircher, K. Kubicek, M. Kunitski, X. Li, T. Mazza, S. Meister, N. Melzer, J. Montano, V. Music, Y. Ovcharenko, C. Passow, A. Pier, N. Rennhack, J. Rist, D. E. Rivas, D. Rolles, I. Schlichting, L. P. H. Schmidt, P. Schmidt, D. Trabert, F. Trinter, R. Wagner, P. Walter, P. Ziolkowski, A. Rudenko, M. Meyer, R. Santra, L. Inhester, T. Jahnke, Imaging collective quantum fluctuations of the structure of a complex molecule. *Science* **389**, 650–654 (2025).

36. Y. Inubushi, G. Yamaguchi, J. Yamada, Y. Kubota, I. Inoue, T. Osaka, T. Yabuuchi, K. Tono, M. Yabashi, Development of portable nanofocusing optics for X-ray free-electron laser pulses. *J. Synchrotron Rad.* **32**, 534–538 (2025).

37. P. Emma, R. Akre, J. Arthur, R. Bionta, C. Bostedt, J. Bozek, A. Brachmann, P. Bucksbaum, R. Coffee, F. J. Decker, Y. Ding, D. Dowell, S. Edstrom, A. Fisher, J. Frisch, S. Gilevich, J. Hastings, G. Hays, P. Hering, Z. Huang, R. Iverson, H. Loos, M. Messerschmidt, A. Miahnahri, S. Moeller, H. D. Nuhn, G. Pile, D. Ratner, J. Rzepiela, D. Schultz, T. Smith, P. Stefan, H. Tompkins, J. Turner, J. Welch, W. White, J. Wu, G. Yocky, J. Galayda, First lasing and operation of an ångstrom-wavelength free-electron laser. *Nat. Photon.* **4**, 641–647 (2010).

38. T. Osipov, C. Bostedt, J. C. Castagna, K. R. Ferguson, M. Bucher, S. C. Montero, M. L. Swiggers, R. Obaid, D. Rolles, A. Rudenko, J. D. Bozek, N. Berrah, The lamp instrument at the linac coherent light source free-electron laser. *Rev. Sci. Instrum.* **89**, 035112 (2018).

39. J. Tersoff, Modeling solid-state chemistry: Interatomic potentials for multicomponent systems. *Phys. Rev. B* **39**, 5566–5568 (1989).

40. K. R. Ferguson, M. Bucher, J. D. Bozek, S. Carron, J. C. Castagna, R. Coffee, G. I. Curiel, M. Holmes, J. Krzywinski, M. Messerschmidt, M. Minitti, A. Mitra, S. Moeller, P. Noonan, T. Osipov, S. Schorb, M. Swiggers, A. Wallace, J. Yin, C. Bostedt, The atomic, molecular and optical science instrument at the linac coherent light source. *J. Synchrotron Radiat.* **22**, 492–497 (2015).

41. L. Strüder, S. Epp, D. Rolles, R. Hartmann, P. Holl, G. Lutz, H. Soltau, R. Eckart, C. Reich, K. Heinzinger, C. Thamm, A. Rudenko, F. Krasniqi, K. U. Kühnel, C. Bauer, C. D. Schröter, R. Moshammer, S. Techert, D. Miessner, M. Porro, O. Hälker, N. Meidinger, N. Kimmel, R. Andritschke, F. Schopper, G. Weidenspointner, A. Ziegler, D. Pietschner, S. Herrmann, U. Pietsch, A. Walenta, W. Leitenberger, C. Bostedt, T. Möller, D. Rupp, M. Adolph, H. Graafsma, H. Hirsemann, K. Gärtner, R. Richter, L. Foucar, R. L. Shoeman, I. Schlichting, J. Ullrich, Large-format, high-speed, x-ray pnCCDs combined with electron and ion imaging spectrometers in a multipurpose chamber for experiments at 4th generation light sources. *Nucl. Instrum. Methods Phys. Res. A* **614**, 483–496 (2010).

42. M. P. Minitti, J. S. Robinson, R. N. Coffee, S. Edstrom, S. Gilevich, J. M. Glownia, E. Granados, P. Hering, M. C. Hoffmann, A. Miahnahri, D. Milathianaki, W. Polzin, D. Ratner, F. Tavella, S. Vetter, M. Welch, W. E. White, A. R. Fry, Optical laser systems at the Linac Coherent Light Source. *J. Synchrotron Radiat.* **22**, 526–531 (2015).

43. X. Lu, L. Feng, T. Akasaka, S. Nagase, Current status and future developments of endohedral metallofullerenes. *Chem. Soc. Rev.* **41**, 7723–7760 (2012).

44. K. R. Ferguson, M. Bucher, T. Gorkhover, S. Boutet, H. Fukuzawa, J. E. Koglin, Y. Kumagai, A. Lutman, A. Marinelli, M. Messerschmidt, K. Nagaya, J. Turner, K. Ueda, G. J. Williams, P. H. Bucksbaum, C. Bostedt, Transient lattice contraction in the solid-to-plasma transition. *Sci. Adv.* **2**, e1500837 (2016).

45. K. R. Ferguson, Crystal structure determination of xenon nanoparticles and x-ray induced transient lattice contraction in the solid-to-plasma transition, Ph.D. thesis, Stanford University (2016). https://stacks.stanford.edu/file/druid:qk328xg1417/Submitted-Dissertation-augmented.pdf.

46. M. Harmand, R. Coffee, M. R. Bionta, M. Chollet, D. French, D. Zhu, D. M. Fritz, H. T. Lemke, N. Medvedev, B. Ziaja, S. Toleikis, M. Cammarata, Achieving few-femtosecond time-sorting at hard x-ray free-electron lasers. *Nat. Photon.* **7**, 215–218 (2013).

47. S. Schorb, T. Gorkhover, J. P. Cryan, J. M. Glownia, M. R. Bionta, R. N. Coffee, B. Erk, R. Boll, C. Schmidt, D. Rolles, A. Rudenko, A. Rouzee, M. Swiggers, S. Carron, J. C. Castagna, J. D. Bozek, M. Messerschmidt, W. F. Schlotter, C. Bostedt, X-ray–optical cross-correlator for gas-phase experiments at the Linac Coherent Light Source free-electron laser. *Appl. Phys. Lett.* **100**, 121107 (2012).

48. B. F. Murphy, T. Osipov, Z. Jurek, L. Fang, S. K. Son, M. Mucke, J. H. D. Eland, V. Zhaunerchyk, R. Feifel, L. Avaldi, P. Bolognesi, C. Bostedt, J. D. Bozek, J. Grilj, M. Guehr, L. J. Frasinski, J. Glownia, D. T. Ha, K. Hoffmann, E. Kukk, B. K. McFarland, C. Miron, E. Sistrunk, R. J. Squibb, K. Ueda, R. Santra, N. Berrah, Femtosecond x-ray-induced explosion of C_{60} at extreme intensity. *Nat. Comm.* **5**, 4281 (2014).

49. U. Saalmann, C. Siedschlag, J. M. Rost, Topical review: Mechanisms of cluster ionization in strong laser pulses. *J. Phys. B At. Mol. Opt. Phys.* **39**, R39 (2006).

50. S. G. Kim, D. Tománek, Melting the fullerenes: A molecular dynamics study. *Phys. Rev. Lett.* **72**, 2418–2421 (1994).

51. A. D. Bandrauk, S. Chelkowski, N. H. Shon, Measuring the electric field of few-cycle laser pulses by attosecond cross correlation. *Phys. Rev. Lett.* **89**, 283903 (2002).

52. H. Li, B. Mignolet, G. Wachter, S. Skruszewicz, S. Zherebtsov, F. Süßmann, A. Kessel, S. A. Trushin, N. G. Kling, M. Kübel, B. Ahn, D. Kim, I. Ben-Itzhak, C. L. Cocke, T. Fennel, J. Tiggesbäumker, K. H. Meiwes-Broer, C. Lemell, J. Burgdörfer, R. D. Levine, F. Remacle, M. F. Kling, Coherent electronic wave packet motion in C_{60} controlled by the waveform and polarization of few-cycle laser fields. *Phys. Rev. Lett.* **114**, 123004 (2015).

53. B. Mignolet, R. D. Levine, F. Remacle, Control of electronic dynamics visualized by angularly resolved photoelectron spectra: A dynamical simulation with an IR pump and xuv attosecond-pulse-train probe. *Phys. Rev. A* **89**, 021403 (2014).

54. T. Yanai, Y. Kurashige, D. Ghosh, G. K.-L. Chan, Accelerating convergence in iterative solution for large-scale complete active space self-consistent-field calculations. *Int. J. Quantum Chem.* **109**, 2178–2190 (2009).

55. B. Mignolet, J. O. Johansson, E. E. B. Campbell, F. Remacle, Probing rapidly-ionizing super-atom molecular orbitals in C_{60}: A computational and femtosecond photoelectron spectroscopy study. *ChemPhysChem* **14**, 3332–3340 (2013).

56. B. Mignolet, R. D. Levine, F. Remacle, Localized electron dynamics in attosecond-pulse-excited molecular systems: Probing the time-dependent electron density by sudden photoionization. *Phys. Rev. A* **86**, 053429 (2012).

57. G. M. Seabra, I. G. Kaplan, V. G. Zakrzewski, J. V. Ortiz, Electron propagator theory calculations of molecular photoionization cross sections: The first-row hydrides. *J. Chem. Phys.* **121**, 4143–4155 (2004).